

COMPTON-THICK AGN IN THE *NuSTAR* ERA III: A SYSTEMATIC STUDY OF THE TORUS COVERING FACTOR

S. MARCHESI¹, M. AJELLO¹, X. ZHAO¹, L. MARCOTULLI¹, M. BALOKOVIĆ², M. BRIGHTMAN³, A. COMASTRI⁴, G. CUSUMANO⁵, G. LANZUISI^{4,6}, V. LA PAROLA⁵, A. SEGRETO⁵, C. VIGNALI^{6,4}

Draft version December 24, 2018

ABSTRACT

We present the analysis of a sample of 35 candidate Compton thick (CT-) active galactic nuclei (AGNs) selected in the nearby Universe (average redshift $\langle z \rangle \sim 0.03$) with the *Swift*-BAT 100-month survey. All sources have available *NuSTAR* data, thus allowing us to constrain with unprecedented quality important spectral parameters such as the obscuring torus line-of-sight column density ($N_{\text{H},z}$), the average torus column density ($N_{\text{H},\text{tor}}$) and the torus covering factor (f_c). We compare the best-fit results obtained with the widely used MYTorus (Murphy & Yaqoob 2009) model with those of the recently published borus02 model (Baloković et al. 2018) used in the same geometrical configuration of MYTorus (i.e., with $f_c=0.5$). We find a remarkable agreement between the two, although with increasing dispersion in $N_{\text{H},z}$ moving towards higher column densities. We then use borus02 to measure f_c . High- f_c sources have, on average, smaller offset between $N_{\text{H},z}$ and $N_{\text{H},\text{tor}}$ than low- f_c ones. Therefore, low f_c values can be linked to a “patchy torus” scenario, where the AGN is seen through an over-dense region in the torus, while high- f_c objects are more likely to be obscured by a more uniform gas distribution. Finally, we find potential evidence of an inverse trend between f_c and the AGN 2–10 keV luminosity, i.e., sources with higher f_c values have on average lower luminosities.

Keywords: galaxies: active — galaxies: nuclei — X-rays: galaxies

1. INTRODUCTION

Obscuration in active galactic nuclei (AGNs) has been largely studied over the electromagnetic spectrum, from the optical (e.g., Lawrence 1991; Simpson 2005), to the infrared (see, e.g., Jaffe et al. 2004; Nenkova et al. 2008), to the X-rays (e.g., Risaliti et al. 1999; Gilli et al. 2007; Marchesi et al. 2016b). Based on the results of these works, it is commonly accepted that the obscuration is caused by a so-called “dusty torus”, i.e., a distribution of molecular gas and dust located at ~ 1 –10 pc from the accreting supermassive black hole (SMBH). While the existence of this obscuring material is universally accepted, its geometrical distribution and chemical composition are still matter of debate, although several works reported that the observational evidence points towards a “patchy torus” scenario, where the obscuring material is distributed in clumps formed by optically thick clouds (e.g., Jaffe et al. 2004; Elitzur & Shlosman 2006; Risaliti et al. 2007; Hönig & Beckert 2007; Nenkova et al. 2008; Risaliti et al. 2011; Burtscher et al. 2013).

With the launch of the Nuclear Spectroscopic Telescope Array (hereafter *NuSTAR*, Harrison et al. 2013), the study and characterization of the physics of the ob-

scuring material surrounding accreting SMBHs experienced a significant step forward. *NuSTAR* is the first telescope with focusing optics at >10 keV, and its sensitivity is almost two orders of magnitude deeper than any of the other previous facilities in the same energy range. Since in the X-rays the observed emission of heavily obscured AGNs peaks at ~ 30 –50 keV (Ajello et al. 2008), where the so-called “Compton hump” is observed, while below 5 keV all the AGN emission is absorbed (Koss et al. 2016), *NuSTAR*, covering the 3–78 keV energy range, represents the ideal instrument to investigate these otherwise elusive sources. The first years of *NuSTAR* were dedicated to the analysis of single, well-known CT-AGNs, or to the characterization of small samples of sources (e.g., Baloković et al. 2014; Puccetti et al. 2014; Annuar et al. 2015; Bauer et al. 2015; Brightman et al. 2015; Koss et al. 2015; Rivers et al. 2015; Masini et al. 2016; Puccetti et al. 2016). By the end of 2017, the sample of heavily obscured AGNs observed by *NuSTAR* was finally large enough to work on a systematic analysis of a statistically significant population of sources.

Consequently, we recently started a project to characterize all the CT-AGNs detected in a volume limited ($d_L < 500$ Mpc, Marchesi et al. 2019 in prep.) sample of bright (observed flux $f_{15-150\text{keV}} \geq 5 \times 10^{-12}$ erg s⁻¹ cm⁻²) AGNs selected in the nearby Universe ($\langle z \rangle = 0.03$) using *Swift*-BAT. As a first step, we analyzed the combined 2–100 keV spectra of 30 sources having an archival *NuSTAR* observation and reported to be CT-AGN in previous works, on the basis of their X-ray spectra. Our main goal was to verify how adding the *NuSTAR* data to the spectral fit improves the general knowledge on the properties of heavily obscured AGNs (Marchesi et al. 2018, hereafter M18). The 2–10 keV data used in this work were obtained from XMM-*Newton*, *Chandra* and *Swift*

¹ Department of Physics and Astronomy, Clemson University, Clemson, SC 29634, USA

² Harvard-Smithsonian Center for Astrophysics, 60 Garden Street, Cambridge, MA 02140, USA

³ Cahill Center for Astrophysics, California Institute of Technology, 1216 East California Boulevard, Pasadena, CA 91125, USA

⁴ Osservatorio di Astrofisica e Scienza dello Spazio di Bologna, Via Piero Gobetti, 93/3, 40129, Bologna, Italy

⁵ INAF - Istituto di Astrofisica Spaziale e Fisica Cosmica, Via U. La Malfa 153, I-90146 Palermo, Italy

⁶ Dipartimento di Fisica e Astronomia, Alma Mater Studiorum, Università di Bologna, Via Piero Gobetti, 93/2, 40129, Bologna, Italy

XRT. The main result of our analysis is the discovery of a systematic offset in the spectral parameters values measured without and with the *NuSTAR* data. We observed a trend to artificially overestimate the line-of-sight column density ($N_{\text{H},z}$) and the steepness of the spectrum when *NuSTAR* data are not included in the fit: this effect is only in small part variability-dependent, since only in three out of 30 sources the fit significantly improved allowing for $N_{\text{H},z}$ to vary between the 2–10 keV and the *NuSTAR* data. Furthermore, we found that the offset is stronger in sources with low statistics (d.o.f.<30) in the 0.3–10 keV+BAT spectrum, i.e., mostly objects with either a *Swift*-XRT or a short (<10 ks) *Chandra* spectrum. In this low-statistics subsample, the intrinsic absorption was overestimated on average by $\sim 40\%$ in the fits without *NuSTAR* data. As a consequence, less than half ($47^{+10}_{-13}\%$) of the candidate CT-AGNs already reported in the literature are confirmed as bona-fide CT-AGNs in our analysis, and 13 out of 30 sources are found to be Compton thin at the $>3\sigma$ confidence level. We point out that our analysis was limited to sources previously reported to be CT-AGNs, therefore it is possible that the opposite trend also exists, i.e., there are sources for which the line-of-sight column density is underestimated fitting only the 2–10 keV+*Swift*-BAT data, and that would be found to be CT-AGNs when adding *NuSTAR* to the fit.

While the results reported in M18 confirmed the fundamental role of *NuSTAR* in characterizing heavily obscured AGNs, their effectiveness in constraining the typical geometrical distribution of the obscuring material around the accreting SMBH was limited by the model used in our analysis, MYTorus (Murphy & Yaqoob 2009; Yaqoob 2012; Yaqoob et al. 2015). In fact, while MYTorus has been proven effective in the X-ray spectral fitting of heavily obscured sources, it also assumes a fixed geometry for its torus model, with a torus half-opening angle $\theta_{\text{OA}}=60^\circ$, i.e., a torus covering factor $f_c=\cos(\theta_{\text{OA}})=0.5$. Immediately after the publication of M18, however, Baloković et al. (2018) published a new torus model, borus02. This model is an updated version of the extensively used BNTorus model (Brightman & Nandra 2011), and has f_c as a free parameter. Notably, f_c is a free parameter also in BNTorus, but Liu & Li (2015) reported that BNTorus has some issues in the geometry-dependent computation of the torus reprocessed component, and should therefore not be used to derive the torus covering factor. Consequently, we decided to reanalyze our sample, this time using borus02, to measure the torus covering factor and study its trend with different AGN parameters, using a statistically significant sample. As of today, the measurement of the torus covering factor from an X-ray perspective has been limited to single sources, mostly observed with *Suzaku* or *NuSTAR* (see, e.g., Awaki et al. 2009; Eguchi et al. 2011; Tazaki et al. 2011; Yaqoob 2012; Kawamuro et al. 2013; Farrah et al. 2016), or small samples of objects (e.g., Brightman et al. 2015; Masini et al. 2016).

This work is organized as follows: in Section 2 we present the sample used in this work and we describe the data reduction and spectral extraction process for both *NuSTAR* and the 0.3–10 keV observations. In Section 3 we describe the models used to perform the spectral fitting. In Section 4 we report the results of the MYTorus

spectral fitting of five sources whose data became public recently, which we did not analyze in M18. In Section 5 we test the recently published borus02 model, comparing its results with those from the MYTorus one, while in Section 6 we use borus02 to measure the torus covering factor (f_c) of the sources in our sample, and we study the f_c trend with $N_{\text{H},z}$ and X-ray luminosity. Finally, we report our conclusions in Section 7. All reported errors are at the 90% confidence level, if not otherwise stated.

2. SAMPLE SELECTION AND DATA REDUCTION

The sources analyzed in this work have been selected from the Palermo BAT 100-month catalog⁷, which reaches a flux limit $f \sim 3.3 \times 10^{-12}$ erg s⁻¹ cm⁻² in the 15–150 keV band. The public data have been first downloaded from the HEASARC public archive and then processed with the BAT_IMAGER code (Segreto et al. 2010). BAT_IMAGER is used to detect sources in observations made using coded mask instruments. The spectra used in our work are background subtracted and exposure-averaged; the spectral redistribution matrix is the official BAT one⁸. The details of the source counterpart association process are reported in Cusumano et al. (2010): we also point out that all the sources in our sample, with the exception of NGC 1358 and ESO 116-G018, have been already reported in previous *Swift*-BAT catalogs (see, e.g., Vasudevan et al. 2013; Ricci et al. 2015, 2017a; Oh et al. 2018). The 100-month catalog (Marchesi et al. 2019 in prep.) contains 1699 sources, less than 10% of which (167) are not associated to a counterpart.

30 out of the 35 sources analyzed in this work were first studied in M18. These sources were selected among the 100-month BAT AGNs which were reported to be CT-AGN in previous works and had available *NuSTAR* archival observation: a detailed summary of all the papers where these objects were first reported to be CT-AGNs is reported in Table 1 of M18. 14 out of 30 sources had 0.5–10 keV coverage from XMM-*Newton*, 2 from *Chandra*, and 14 from *Swift*-XRT. Notably, for the majority of these sources the line-of-sight column density measurement was originally obtained using only 0.5–10 keV data, in some cases with the further addition of BAT information in the 15–150 keV band, but without using *NuSTAR*.

In this paper, we reanalyze all the 30 sources we studied in M18, and we add to the sample five other candidate CT-AGNs from the 100-month BAT catalog with available *NuSTAR* data that were not studied in the previous work. We report in Table 1 a summary of these five new sources.

2.1. Data reduction for the five sources not reported in Marchesi et al. (2018)

The five sources not analyzed in M18 are ESO 116-G018 ($z=0.0185$), NGC 1358 ($z=0.0134$), Mrk 3 ($z=0.0254$), MCG-01-30-041 ($z=0.0188$) and NGC 7479 ($z=0.0079$).

NGC 1358 and ESO 116-G018 were first analyzed in Marchesi et al. (2017) using *Chandra* data. Both sources

⁷ http://bat.ifc.inaf.it/100m_bat_catalog/100m_bat_catalog_v0.0.htm

⁸ <http://heasarc.gsfc.nasa.gov/docs/heasarc/caldb/data/swift/bat/index.html>

were found to have $N_{\text{H,z}} \sim 10^{24} \text{ cm}^{-2}$. Therefore, we proposed for a joint *NuSTAR*–XMM–*Newton* observation of both these objects, to properly characterize them. Our proposal was accepted (*NuSTAR* GO Cycle 3, proposal ID: 3258; PI S. Marchesi) and we were granted *NuSTAR* (50 ks for both sources) and XMM–*Newton* (50 ks for ESO 116-G018 and 45 ks for NGC 1358) time. The results of the spectral analysis have been published in Zhao et al. (2018b,a). For these two sources, as well as for Mrk 3 and NGC 7479, we reduced the XMM–*Newton* data using the SAS v16.0.0⁹ packages and adopting standard procedures. The source spectra were extracted from a 15'' circular region, corresponding to $\sim 70\%$ of the encircled energy fraction at 5 keV for all the three XMM–*Newton* 0.5–10 keV cameras (MOS1, MOS2 and pn), while the background spectra were obtained from a circle having radius 45'' located near the source and not contaminated by nearby objects. Each spectrum has been binned with at least 20 counts per bin.

MCG–01–30–041 has only been observed twice with *Swift*-XRT in the 0.5–10 keV band: since one of these observations was taken simultaneously with the *NuSTAR* one, we used this in our analysis, to reduce potential variability issues. We obtained the *Swift*-XRT spectrum using the *Swift* products generator available online (http://www.swift.ac.uk/user_objects/; see also Evans et al. 2009). Due to the spectrum low statistics, we binned it with only 3 counts per bin and we therefore analyzed it using the `cstat`, rather than the χ^2 , statistic (see Section 4).

Finally, for all five objects the data retrieved for both *NuSTAR* Focal Plane Modules (FPMA and FPMB; Harrison et al. 2013) were processed using the *NuSTAR* Data Analysis Software (NUSTARDAS) v1.5.1. The event data files were calibrated running the `nupipeline` task using the response file from the Calibration Database (CALDB) v. 20180419. With the `nuproducts` script we generated both the source and background spectra, and the ancillary and response matrix files. For both focal planes, we used a circular source extraction region with a 30'' radius, corresponding to $\sim 50\%$ of the encircled energy fraction over the whole *NuSTAR* energy range, and centered on the target source; for the background we used the same extraction region positioned far from any source contamination in the same frame. The *NuSTAR* spectra have then been grouped with at least 20 counts per bin, and cover the energy range from 3 to 50–70 keV, depending on the quality of the data.

3. SPECTRAL FITTING PROCEDURE

The spectral fitting procedure was performed using the XSPEC software (Arnaud 1996); the Galactic absorption values is the one measured by Kalberla et al. (2005). We used Anders & Grevesse (1989) cosmic abundances, fixed to the solar value, and the Verner et al. (1996) photoelectric absorption cross-section. Following the same approach described in M18, we fit our data in the 2–150 keV regime, since in heavily obscured AGNs the 0.5–2 keV band emission is dominated by non-AGN processes, such as star-formation and/or diffuse gas emission (see, e.g., Koss et al. 2015).

Heavily obscured AGNs have complex spectra, where

the contribution of the Compton scattering and of the fluorescent Iron line becomes significant with respect to less obscured AGN spectra. Consequently, these sources should be treated in a self-consistent way, that allows one to properly measure $N_{\text{H,z}}$, using models developed specifically to this purpose. In M18, we fitted the 30 sources in our sample with a Monte Carlo radiative transfer code: `MYTorus` (Murphy & Yaqoob 2009; Yaqoob 2012; Yaqoob et al. 2015). In this work we use both `MYTorus` and `borus02` (Baloković et al. 2018), another Monte Carlo radiative transfer code. More in detail, we first fit the spectra of the five sources not reported in M18 using `MYTorus`. We then fit with `borus02` both the 30 sources in M18 and the five new sources, using two distinct model configurations: the first one with `borus02` in the same geometrical configuration than `MYTorus`, the second one allowing the torus covering factor to vary.

3.1. *MYTorus*

The `MYTorus` model is divided in three distinct components.

1. A multiplicative component containing photoelectric absorption and Compton scattering attenuation, with associated equivalent neutral hydrogen column density ($N_{\text{H,z}}$). This component is applied to the main power law continuum.
2. A scattered continuum, also known as “reprocessed component”. This component models those photons that are observed after one or more interactions with the material surrounding the SMBH. The normalization of the reprocessed component with respect to the main continuum hereby denoted as A_{S} .
3. The neutral Fe fluorescent emission lines, more in detail the Fe $K\alpha$ line at 6.4 keV and the $K\beta$ at 7.06 keV. We denote the normalization of these lines with respect to the main continuum as A_{L} .

In `MYTorus`, the obscuring material surrounding the SMBH is assumed to have a toroidal, azimuthally symmetric shape. The torus covering factor, f_c , is not a free parameter and is fixed to $f_c = \cos(\theta_{\text{OA}}) = 0.5$, where $\theta_{\text{OA}} = 60^\circ$ is the torus half-opening angle. The angle between the torus axis and the observer is free to vary, within the range $\theta_{\text{obs}} = [0-90]^\circ$. In our analysis, both in M18 and here, we use `MYTorus` in the so-called “decoupled mode” (Yaqoob et al. 2015): for the main continuum, we fix $\theta_{\text{obs}} = 90^\circ$, while for the reprocessed component we test two different scenarios, one with $\theta_{\text{obs,AS,AL}} = 90^\circ$, the other with $\theta_{\text{obs,AS,AL}} = 0^\circ$, checking which one leads to the smaller reduced χ^2 , $\chi^2_{\nu} = \chi^2 / (\text{degrees of freedom})$. Sources best-fitted with $\theta_{\text{obs,AS,AL}} = 90^\circ$ correspond to a scenario where the dense obscuring torus is observed “edge-on” and the obscuring material lies between the AGN and the observer. Sources best-fitted with $\theta_{\text{obs,AS,AL}} = 0^\circ$, instead, are assumed to describe a patchy torus scenario, in which the reprocessed emission from the inner edge of the torus can reach the observer.

⁹ <http://xmm.esa.int/sas>

4PBC name	Source name	R.A. deg	Decl deg	Type	z	Telescope	ObsID	Date	Exposure ks	Rate cts s ⁻¹	Ref.
(1)	(2)	(3)	(4)	(5)	(6)	(7)	(8)	(9)	(10)	(11)	(12)
J0324.8-6043	ESO 116-G018	51.2210	-60.7384	2	0.0185	XMM- <i>Newton</i>	0795680201	2017-11-01	164.8	0.015	(a)
...	<i>NuSTAR</i>	60301027002	2017-11-01	90.1	0.013	-
J0333.7-0504	NGC 1358	53.4153	-5.0894	2	0.0134	XMM- <i>Newton</i>	0795680101	2017-08-01	100.6	0.014	(a)
...	<i>NuSTAR</i>	60301026002	2017-08-01	99.8	0.023	-
J0615.5+7102	Mrk 3	93.90129	71.037476	2	0.0254	XMM- <i>Newton</i>	0741050501	2015-04-06	19.9	0.089	(b)
...	<i>NuSTAR</i>	60002048004	2014-09-14	66.9	0.049	(c)*
J1152.7-0511	MCG-01-30-041	178.15887	-5.206967	1.8	0.0188	<i>Swift</i> -XRT	80062	2017-06-14	7.1	0.065	(d)
...	<i>NuSTAR</i>	60061216002	2017-06-14	53.7	0.086	-
J2304.7+1219	NGC 7479	346.236042	12.322889	2	0.0079	XMM- <i>Newton</i>	0025541001	2001-06-19	29.9	0.041	(e)
...	<i>NuSTAR</i>	60201037002	2016-05-12	36.9	0.015	-

Table 1

Candidate CT-AGNs analyzed in this work and not reported in M18. Column (1): ID from the Palermo BAT 100-month catalog (Marchesi et al. 2019 in prep.). (2): source name. (3) and (4): right ascension and declination (J2000 epoch). (5): optical classification (1.8: Seyfert 1.8 galaxy; 2: Seyfert 2 galaxy). (6): redshift. (7): telescope used in the analysis. (8): observation ID. (9): observation date. (10): total exposure, in ks. For XMM-*Newton* and *NuSTAR*, this is the sum of the exposures of each camera. (11): average count rate (in cts s⁻¹), weighted by the exposure for XMM-*Newton* and *NuSTAR*, where observations from multiple instruments are combined. Count rates are computed in the 3–70 keV band for *NuSTAR* and in the 2–10 keV band otherwise. (12): reference for previous assessments of CT nature for the source, as follows. When *NuSTAR* data were used, the reference is reported on the *NuSTAR* observation line. Sources previously fitted with a torus model are flagged with a *. a) Marchesi et al. (2017); b) Cappi et al. (1999); c) Guainazzi et al. (2016); d) Vasudevan et al. (2013); e) Severgnini et al. (2012).

3.2. *borus02*

borus02 (Baloković et al. 2018) is an updated and improved version of the widely used **BNTorus** model (Brightman & Nandra 2011). This radiative transfer code models the reprocessed emission component of an AGN X-ray spectrum, i.e., following the **MYTorus** nomenclature we introduced in the previous section, the “reprocessed component” and the neutral Fe emission lines.

In **borus02**, the obscuring material has a quasi-toroidal geometry, with conical polar cutouts. Both the average torus column density ($N_{\text{H,tor}}$) and the torus covering factor are free parameters in the model: the torus covering factor value can vary in the range $f_c=[0.1-1.0]$, corresponding to a torus opening angle range $\theta_{\text{OA}}=[0-84]^\circ$. In principle, the angle between the torus axis and the observer is also a free parameter of this model, but in our analysis we fix it to $\theta_{\text{obs}}=87^\circ$, i.e., the upper boundary of the parameter in the model, corresponding to an almost “edge-on” configuration. In this work, we decide to fix θ_{obs} to reduce potential degeneracies between this parameter, $N_{\text{H,tor}}$ and f_c , particularly in sources with low statistics (i.e., with less than 150–200 degrees of freedom). We are also working on a companion paper (Zhao et al. 2019 in prep.) where we use a sample of nearby AGNs, both obscured and unobscured, to analyze how leaving θ_{obs} free to vary affects the other spectral parameters.

Finally, since the **borus02** models itself does not take into account line-of-sight absorption, we follow Baloković et al. (2018) approach and derive $N_{\text{H,z}}$ in XSPEC using the components **zphabs** × **cabs** to properly model Compton scattering losses out of the line of sight. In the overall fitting model, the $N_{\text{H,z}}$ value is a free parameter, independent from $N_{\text{H,tor}}$, and assumed to be identical in **zphabs** and **cabs**.

3.3. Additional components to the best-fit model

Besides using **MYTorus** and **borus02** in the configurations described in the previous sections, we included the following components to our best-fit model:

1. A second power law, with photon index $\Gamma_2=\Gamma_1$, where Γ_1 is the photon index of the primary power law. This second power law is introduced to take into account the fraction f_{scatt} of accreting SMBH emission which is scattered, rather than absorbed, by the gas surrounding the SMBH. We assume this component to be unabsorbed.
2. A constant, $C_{\text{NuS-2-10}}$, allowing for a renormalization of the *NuSTAR* spectrum with respect to the 2–10 keV + *Swift*-BAT one. Such a component models both cross-calibration offsets between the 2-10 keV and the *NuSTAR* data and potential flux variability between the different observations.
4. **MYTorus** FITTING RESULTS FOR THE FIVE SOURCES NOT REPORTED IN MARCHESI ET AL. (2018)

As a first step of our analysis, we fitted with **MYTorus** the five sources which we did not report in M18: we jointly fitted the 2–10 keV (from either XMM-*Newton*, *Chandra* or *Swift*-XRT), *NuSTAR* and *Swift*-BAT data, and the **MYTorus** configuration is the one described in Section 3.1. All sources but NGC 7479 are fitted using the χ^2 statistic: due to its low 2–10 keV count statistics, we measure the goodness of the fit in NGC 7479 with the W statistic (**cstat** in XSPEC), which is commonly used when a source does not have enough counts to be fitted with the χ^2 method. However, the *Swift*-BAT spectra are already background-subtracted and can therefore not be fitted with **cstat**: for this reason, we used the multi-statistic approach allowed by XSPEC and fitted the *Swift*-BAT data with the χ^2 statistic. The best-fit statistic we report for NGC 7479 in Table 2 is thus the sum of **cstat** and χ^2 .

In Table 2 we also report the best-fit parameters for our new five sources: $N_{\text{H,z}}$, Γ , the 2–10 keV to *NuSTAR* cross-normalization constant, $C_{\text{NuS-2-10}}$; the main power law component normalization, norm_1 ; the reprocessed and iron lines relative normalizations, A_S and A_L ; the fraction of scattered emission, f_{scatt} . The observed flux and the intrinsic luminosity in the 2–10 keV

and in the 15–55 keV band are also reported. For all five sources, we find that the best-fit model is the one with $\theta_{\text{obs,AS,AL}}=90^\circ$.

Three out of five sources (ESO 116-G018, NGC 1358 and NGC 7479) are confirmed to be CT-AGN at a $>3\sigma$ level. A fourth source, Mrk 3, is found to have best-fit line-of-sight column density $N_{\text{H,z}}=(7.8\pm 0.1)\times 10^{23}\text{ cm}^{-2}$, slightly below the CT threshold. However, this is not an unexpected result, since this source is known to be highly variable, a result confirmed also in our analysis, since we find $C_{\text{NuS-2-10}}=2.07^{+0.02}_{-0.04}$. A Compton-thin solution for this source was already reported in Yaqoob et al. (2015); furthermore, a recent monitoring campaign with *NuSTAR* performed by Guainazzi et al. (2016) showed that the line-of-sight column density of Mrk 3 varied in the range $N_{\text{H,z}}=[0.75\text{--}0.94]\times 10^{24}\text{ cm}^{-2}$ in a timespan of seven months. Notably, there is an excellent agreement between our $N_{\text{H,z}}$ measurement and the one obtained by Guainazzi et al. (2016) using the same *NuSTAR* observation, i.e., $N_{\text{H,z}}=(7.7\pm 0.1)\times 10^{23}\text{ cm}^{-2}$.

Finally, we find that MCG-01-30-041, which was reported to be a CT-AGN ($N_{\text{H,z}}=1.45^{+0.74}_{-0.45}\times 10^{24}\text{ cm}^{-2}$) by Vasudevan et al. (2013), is in fact an unobscured AGN ($N_{\text{H,z}}<10^{22}\text{ cm}^{-2}$) based on our combined *Swift*-XRT, *Swift*-BAT and *NuSTAR* fit. Notably, we find that even fitting the *Swift*-XRT and *Swift*-BAT data only does not produce a CT solution, the best-fit line-of-sight column density being in this case $N_{\text{H,z}}=1.8^{+2.1}_{-1.1}\times 10^{23}\text{ cm}^{-2}$, with a corresponding power law photon index $\Gamma=2.13^{+0.44}_{-0.37}$. The reason of the discrepancy between our result and the one reported by Vasudevan et al. (2013) is likely linked to the very low quality of the combined *Swift*-XRT and *Swift*-BAT spectrum used in their work: the *Swift*-XRT spectrum used in their analysis has in fact only ~ 30 counts in the 2–10 keV band (our combined *Swift*-XRT and *NuSTAR* spectrum has ~ 3850 counts in the same band), and their fit has only 6 degrees of freedom (ours has 297).

We report in Figure 1 the 2–100 keV spectra of the five sources, as well as the corresponding best-fit models.

5. COMPARISON BETWEEN MYTORUS AND BORUS02

In order to validate the reliability of the **borus02** model and use it to measure the torus covering factor, in this section we compare the results obtained using **MYTORUS** with those obtained using **borus02** with the same geometrical configuration of **MYTORUS**, i.e., fixing the torus covering factor to $f_c=0.5$ ($\theta_{\text{OA}}=60^\circ$) and the angle between the observer and the torus axis to $\theta_{\text{obs}}=87^\circ$, i.e., the maximum value allowed by **borus02**¹⁰. We also fix the strength of the reprocessed component, A_S , to the best-fit value we obtained using **MYTORUS** (see Table 2 and Table 3 in M18). The overall torus column density, $\log(N_{\text{H,tor}})$, is left free to vary.

In Table 3 we report the best-fit, line-of-sight column density and photon index values for the 35 sources in our sample, using either **MYTORUS** or **borus02**, while in Figure 2 we show the trends of these parameters obtained using **borus02** as a function of those obtained using **MYTORUS**.

¹⁰ While in M18 we used $\theta_{\text{obs}}=90^\circ$, we checked that the difference in the best-fit values of Γ and $N_{\text{H,z}}$ using $\theta_{\text{obs}}=90^\circ$ and $\theta_{\text{obs}}=87^\circ$ is $<1\%$

As can be seen in Figure 2, left panel, there is a general excellent agreement between the $N_{\text{H,z}}$ value obtained using **borus02** and the one obtained using **MYTORUS**: the best-fit slope of the relation $\log(N_{\text{H,z,Borus}})=a\log(N_{\text{H,z,MyT}})+b$ is $a=0.97\pm 0.05$, and the Spearman rank order correlation coefficient of the distribution is $\rho=0.90$, and the p-value for such a ρ value to be derived by an uncorrelated population is $p=1.2\times 10^{-12}$. However, the high overall correlation observed in the whole sample hides the existence of two clear separate trends: sources having $N_{\text{H,z}}\leq 10^{24}\text{ cm}^{-2}$ based on both the **MYTORUS** and the **borus02** best-fit have excellent correlation, the Spearman rank order correlation coefficient being $\rho=0.92$ (p-value $p=1.1\times 10^{-6}$). On the opposite, we find a weaker correlation for sources being CT- according to at least one of the two models: in this second scenario, the sample has $\rho=0.49$ and p-value $p=0.04$. We also find that one source (NGC 1194), is found to be CT using **borus02** and has instead $N_{\text{H,z,MyT}}<10^{24}\text{ cm}^{-2}$, while another object (MCG+06-16-028) is a CT-AGN with **MYTORUS** but has $N_{\text{H,z,Borus}}<10^{24}\text{ cm}^{-2}$, although for this source the two $N_{\text{H,z,MyT}}$ measurements are consistent at the 90% confidence level.

The larger dispersion observed in the Compton thick regime is not unexpected, since above the CT threshold the $N_{\text{H,z}}$ measurement becomes more complex, because of the slightly different geometries of the models. Nonetheless, it is worth noticing that for 11 out of the 16 sources being confirmed CT-AGNs based on both **MYTORUS** and **borus02** have $N_{\text{H,z}}$ values in agreement at the 90% confidence level.

In Figure 2, right panel, we plot the best-fit photon index obtained using **borus02**, as a function of the same parameter obtained using **MYTORUS**. Sources classified as CT-AGNs by either **MYTORUS** or **borus02** are plotted in red, while sources with $N_{\text{H,z}}<10^{24}\text{ cm}^{-2}$ in both models are plotted in black. As can be seen, the dispersion of the distribution is quite large, the Spearman rank order correlation coefficient being $\rho=0.64$ and the p-value for such a ρ value to be derived by an uncorrelated population is $p=6.8\times 10^{-5}$. However, the overall agreement between the two models is remarkable, the average photon index measured with **MYTORUS** being $\langle\Gamma_{\text{MyT}}\rangle=1.74$, with associated standard deviation $\sigma_{\Gamma_{\text{MyT}}}=0.16$, while the average photon index measured using **borus02** is $\langle\Gamma_{\text{Borus}}\rangle=1.69$, with associated standard deviation $\sigma_{\Gamma_{\text{Borus}}}=0.15$. Furthermore, 29 out of 35 sources (i.e., 83% of the objects in our sample) have Γ_{Borus} consistent with Γ_{MyT} within the 90% confidence uncertainty. We point out that measuring Γ with such a high accuracy in CT-AGNs is a remarkable result, since in such obscured objects the intrinsic power-law continuum is not directly observable in any part of the spectrum below 5–10 keV.

In conclusion, our analysis shows that, when using **borus02** in a geometrical configuration consistent with the **MYTORUS** one, the best-fit results from the two models are in good agreement. Such an evidence supports the main goal of this work, i.e., using **borus02** to measure the obscuring material covering factor for the 35 objects in our sample.

6. CONSTRAINING THE TORUS COVERING FACTOR

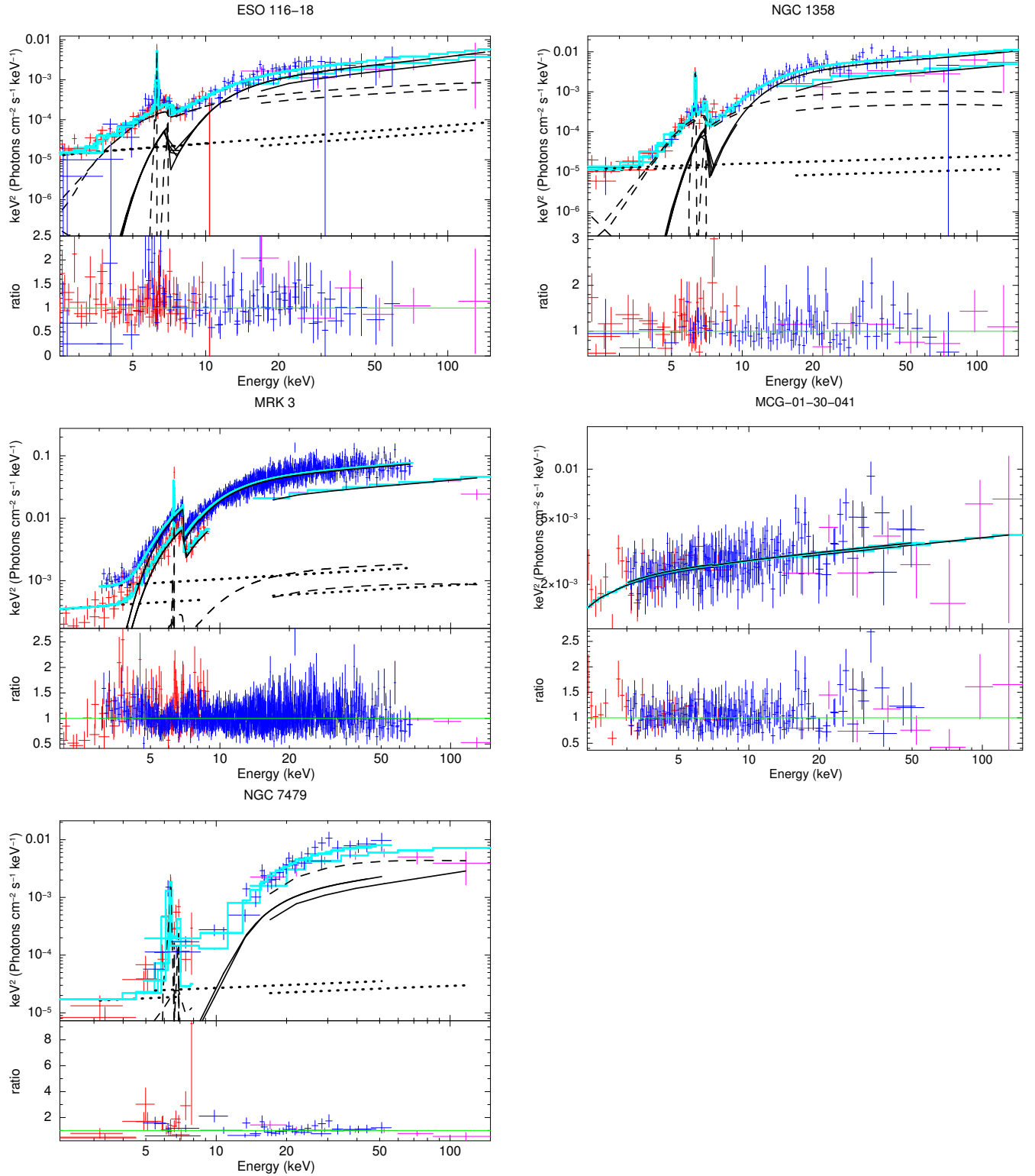


Figure 1. Background-subtracted spectra (top panel) and data-to-model ratio (bottom) of the five CT-AGNs analyzed in this work and not previously analyzed in M18. 2–10 keV data are plotted in red, *NuSTAR* data in blue and *Swift*-BAT data in magenta. The best-fitting model is plotted as a cyan solid line, while the single MYTorus components are plotted as black solid (zeroth-order continuum) and dashed (reprocessed component and emission lines) lines. Finally, the main power law component scattered, rather than absorbed, by the torus is plotted as a black dotted line.

Source	$N_{\text{H},z}$	Γ	$C_{\text{NuS-2-10}}$	norm ₁	A_{S} %	f_{scatt}	f_{2-10}	L_{2-10}	f_{15-55}	L_{15-55}	$\chi^2/\text{d.o.f.}$
ESO 116-G018	$190.0^{+76.0}_{-33.0}$	$1.55^{+0.18}_{-0.15}$	$1.05^{+0.14}_{-0.13}$	$18.52^{+14.89}_{-6.13}$	$0.84^{+0.39}_{-0.37}$	$0.5^{+0.3}_{-0.2}$	$-12.52^{+0.03}_{-0.09}$	$43.30^{+0.47}_{-0.42}$	$-11.34^{+0.02}_{-0.13}$	$43.19^{+0.19}_{-0.19}$	187.0/210
NGC 1358	$236.0^{+27.0}_{-33.0}$	$1.82^{+0.24}_{-0.26}$	$1.17^{+0.15}_{-0.14}$	$141.32^{+42.21}_{-31.33}$	$0.25^{+0.06}_{-0.05}$	$0.1^{+0.1}_{-0.1}$	$-12.41^{+0.02}_{-0.05}$	$43.39^{+0.21}_{-0.33}$	$-10.95^{+0.02}_{-0.03}$	$43.39^{+0.11}_{-0.10}$	220.0/239
Mrk 3	$78.9^{+2.3}_{-2.1}$	$1.78^{+0.02}_{-0.02}$	$2.06^{+0.05}_{-0.05}$	$240.64^{+25.53}_{-13.93}$	<0.30	$1.3^{+0.2}_{-0.1}$	$-11.18^{+0.03}_{-0.02}$	$44.04^{+0.04}_{-0.04}$	$-9.91^{+0.03}_{-0.02}$	$44.23^{+0.03}_{-0.03}$	1183.4/1098
MCG-01-30-041	<1.0	$1.85^{+0.05}_{-0.04}$	$1.03^{+0.09}_{-0.08}$	$18.59^{+2.87}_{-1.94}$	–	–	$-11.26^{+0.02}_{-0.07}$	$42.64^{+0.03}_{-0.04}$	$-11.17^{+0.03}_{-0.04}$	$42.71^{+0.01}_{-0.01}$	222.2/225
NGC 7479	$363.6^{+58.0}_{-50.3}$	$1.83^{+0.09}_{-0.09}$	$1.34^{+0.22}_{-0.20}$	$110.08^{+44.50}_{-33.92}$	1.00 ^f	<0.5	$-12.75^{+0.04}_{-0.08}$	$42.64^{+0.14}_{-0.18}$	$-10.96^{+0.04}_{-0.07}$	$43.00^{+0.26}_{-0.66}$	200.6/171

Table 2

Best fit properties for the five new candidate CT-AGNs analyzed in this work and not reported in M18. The reported parameters have been obtained by fitting all the available data for the given source, including *NuSTAR*. $N_{\text{H},z}$ is the line-of-sight column density (in units of 10^{22} cm^{-2}); Γ is the power law photon index; $C_{\text{NuS-2-10}}$ is the cross-normalization constant between the 2–10 keV and the *NuSTAR* data; norm₁ is the main power law normalization (in units of $\text{ph cm}^2 \text{ s}^{-1} \text{ keV}^{-1} \times 10^{-4}$), measured at 1 keV; A_{S} is the intensity of the MYtorus reprocessed component with respect to the main one; f_{scatt} is the percentage of main power law emission scattered, rather than absorbed, by the obscuring material. f_{2-10} , L_{2-10} , f_{15-55} and L_{15-55} are the logarithms of the observed flux (in units of $\text{erg s}^{-1} \text{ cm}^{-2}$) and the intrinsic, unabsorbed luminosity (in units of erg s^{-1}) measured in the 2–10 keV and in the 15–55 keV bands, respectively. Fluxes and luminosities are obtained with XSPEC, using the flux command and the clumin convolution model, respectively. Parameters fixed to a given value are flagged with ^f. The intensity of the Iron lines, A_{L} , is assumed to be $=A_{\text{S}}$ in all sources but NGC 7479, where is $A_{\text{L}}=4.44^{+1.24}_{-1.02}$. We find MCG-01-30-041 to be an unobscured AGN, therefore the fit did not required neither the reprocessed component A_{S} nor the scattered component f_{scatt} .

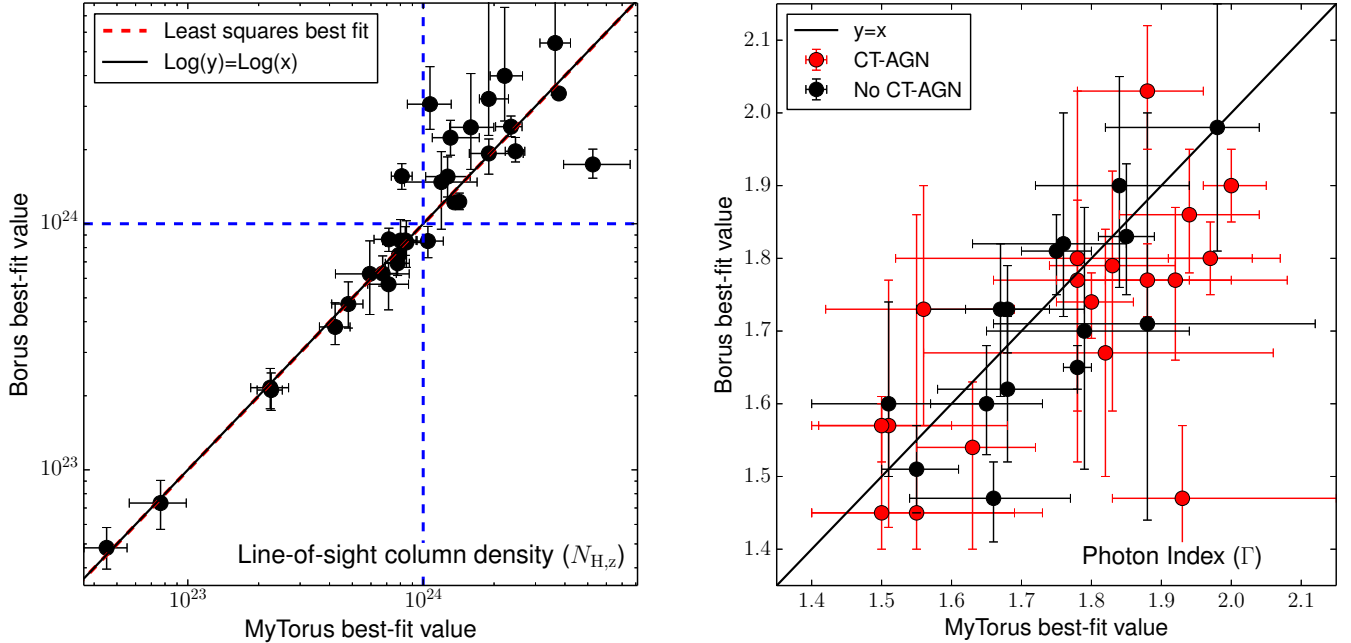


Figure 2. *Left:* Distribution of the line-of-sight column density $N_{\text{H},z}$ measured using the borus02 model as a function of the same parameter measured using the MYtorus model. NGC 1068, which has $N_{\text{H},z} > 10^{25} \text{ cm}^{-2}$, and RBS 1037 and MCG-01-30-041, which we find to be unobscured AGNs, are not shown in the plot. The $\log(y)=\log(x)$ relation is plotted as a black solid line, while the best-fit relation $\log(N_{\text{H},z,\text{Borus}})=a+b\log(N_{\text{H},z,\text{Borus}})$ is plotted as a red dashed line. The blue dashed horizontal and vertical lines mark the CT threshold, $N_{\text{H},z}=10^{24} \text{ cm}^{-2}$. *Right:* same as left, but for the photon index Γ . Source with $N_{\text{H},z} > 10^{24} \text{ cm}^{-2}$ from either the MYtorus or the borus02 model are plotted in red, while sources with $N_{\text{H},z} < 10^{24} \text{ cm}^{-2}$ in both models are plotted in black. Here, we do not plot NGC 1229, whose Γ_{NuS} value is pegged to $\Gamma=1.4$, the MYtorus model’s lower boundary. The $y=x$ relation is plotted as a black solid line.

Source	MYTorus			borus02		
	$N_{\text{H},z}$ 10^{22} cm^{-2}	Γ	χ^2/DOF	$N_{\text{H},z}$ 10^{22} cm^{-2}	Γ	χ^2/DOF
NGC 424	$130.6^{+42.5}_{-21.3}$	$1.51^{+0.17}_{-0.11l}$	429.8/335	$223.7^{+39.5}_{-33.9}$	$1.57^{+0.20}_{-0.14}$	398.6/334
MCG+08-03-018	$47.9^{+7.4}_{-7.2}$	$1.84^{+0.10}_{-0.12}$	176.9/151	$46.9^{+10.9}_{-9.5}$	$1.90^{+0.15}_{-0.14}$	169.5/150
NGC 1068 ^N	$1000.0^{+0.0u}_{-142.8}$	$1.88^{+0.08}_{-0.10}$	602.5/552	1000.0 ^f	$2.03^{+0.09}_{-0.08}$	664.7/551
NGC 1194	$81.1^{+8.6}_{-7.9}$	$1.50^{+0.10}_{-0.09}$	307.5/244	$156.1^{+19.4}_{-18.1}$	$1.57^{+0.04}_{-0.05}$	272.9/243
NGC 1229	$42.3^{+6.6}_{-6.0}$	1.40 ^f	98.5/97	$38.1^{+9.7}_{-5.8}$	$1.47^{+0.14}_{-0.07l}$	95.4/96
ESO 116-G018	$190.0^{+76.0}_{-33.0}$	$1.55^{+0.18}_{-0.15l}$	187.0/210	$193.0^{+34.0}_{-28.0}$	$1.45^{+0.41}_{-0.05l}$	190.0/209
NGC 1358	$236.0^{+27.0}_{-33.0}$	$1.82^{+0.24}_{-0.26}$	220.0/239	$248.0^{+40.0}_{-46.0}$	$1.67^{+0.17}_{-0.17}$	230.0/238
ESO 201-IG004	$71.3^{+15.4}_{-13.1}$	$1.51^{+0.14}_{-0.11l}$	108.7/84	$56.8^{+12.7}_{-12.1}$	$1.60^{+0.14}_{-0.10}$	104.7/83
2MASXJ03561995-6251391	$83.9^{+9.4}_{-10.5}$	$1.98^{+0.06}_{-0.16}$	134.5/138	$85.1^{+11.8}_{-11.2}$	$1.98^{+0.18}_{-0.17}$	132.3/137
CGCG 420-15	$71.5^{+8.5}_{-9.7}$	$1.66^{+0.11}_{-0.12}$	268.6/219	$86.4^{+9.5}_{-9.3}$	$1.47^{+0.05}_{-0.06}$	260.0/218
MRK 3	$78.9^{+2.3}_{-2.1}$	$1.78^{+0.02}_{-0.02}$	1183.4/1098	$74.7^{+2.2}_{-1.7}$	$1.65^{+0.03}_{-0.03}$	1142.4/1097
ESO 005-G004	$106.9^{+24.7}_{-21.2}$	$1.63^{+0.09}_{-0.08}$	86.0/72	$306.1^{+128.7}_{-64.2}$	$1.54^{+0.09}_{-0.14l}$	87.2/71
MCG+06-16-028	$104.7^{+17.0}_{-17.3}$	$1.56^{+0.13}_{-0.14}$	82.3/87	$85.0^{+12.5}_{-12.3}$	$1.73^{+0.17}_{-0.16}$	76.3/86
2MASXJ09235371-3141305	$67.3^{+9.6}_{-9.6}$	$1.76^{+0.09}_{-0.13}$	193.7/145	$62.8^{+11.2}_{-7.0}$	$1.82^{+0.18}_{-0.10}$	182.2/144
NGC 3079	$246.7^{+23.5}_{-23.5}$	$1.94^{+0.10}_{-0.10}$	206.9/182	$197.0^{+27.2}_{-18.7}$	$1.86^{+0.09}_{-0.08}$	204.1/181
NGC 3393	$189.7^{+40.5}_{-16.5}$	$1.78^{+0.22}_{-0.12}$	66.7/92	$321.6^{+678.4}_{-93.1}$	$1.77^{+0.11}_{-0.18}$	54.8/91
2MASXJ10523297+1036205	$7.7^{+2.2}_{-2.0}$	$1.55^{+0.06}_{-0.05}$	545.8/515	$7.3^{+1.7}_{-1.6}$	$1.51^{+0.06}_{-0.06}$	534.9/514
RBS 1037	<1.0	$1.75^{+0.05}_{-0.05}$	315.6/313	<0.2	$1.81^{+0.05}_{-0.06}$	319.7/312
MCG-01-30-041	<1.0	$1.85^{+0.05}_{-0.04}$	222.2/225	<1.5	$1.83^{+0.10}_{-0.09}$	220.1/224
NGC 4102	$77.8^{+9.5}_{-8.8}$	$1.67^{+0.12}_{-0.12}$	217.5/191	$69.1^{+7.3}_{-7.5}$	$1.73^{+0.09}_{-0.12}$	204.1/190
B2 1204+34	$4.5^{+1.0}_{-0.9}$	$1.68^{+0.06}_{-0.06}$	222.5/248	$4.8^{+1.0}_{-0.9}$	$1.73^{+0.06}_{-0.06}$	217.3/247
NGC 4945	$377.0^{+16.6}_{-15.7}$	$1.97^{+0.06}_{-0.06}$	1508.8/1486	$338.3^{+11.1}_{-9.2}$	$1.80^{+0.05}_{-0.05}$	1543.5/1485
NGC 5100	$22.6^{+2.6}_{-2.9}$	$1.68^{+0.10}_{-0.10}$	191.4/197	$21.1^{+3.7}_{-3.7}$	$1.62^{+0.10}_{-0.10}$	191.8 /196
IGR J14175-4641	$80.1^{+14.0}_{-12.9}$	$1.79^{+0.15}_{-0.14}$	84.3/80	$85.4^{+18.6}_{-17.4}$	$1.70^{+0.17}_{-0.19}$	83.6/79
NGC 5643	$159.4^{+40.2}_{-29.8}$	$1.93^{+0.22}_{-0.10}$	154.0/137	$246.4^{+161.2}_{-80.2}$	$1.47^{+0.10}_{-0.07l}$	153.9/136
MRK 477	$22.4^{+4.4}_{-3.9}$	$1.65^{+0.08}_{-0.08}$	245.9/227	$21.6^{+4.3}_{-3.9}$	$1.60^{+0.08}_{-0.07}$	260.2/226
NGC 5728	$142.3^{+8.6}_{-8.7}$	$1.88^{+0.06}_{-0.06}$	362.4/329	$123.0^{+10.3}_{-8.9}$	$1.77^{+0.05}_{-0.05}$	363.6/328
CGCG 164-019	$119.5^{+50.0}_{-36.2}$	$1.78^{+0.29}_{-0.26}$	59.9/58	$147.7^{+48.6}_{-52.7}$	$1.80^{+0.23}_{-0.28}$	59.6/57
NGC 6232	$59.3^{+27.9}_{-16.9}$	$1.44^{+0.34}_{-0.04l}$	35.9/34	$62.6^{+22.7}_{-19.8}$	1.40 ^f	36.1/33
NGC 6240	$135.5^{+6.5}_{-6.4}$	$1.80^{+0.06}_{-0.05}$	533.8/496	$122.2^{+7.2}_{-6.6}$	$1.74^{+0.04}_{-0.05}$	520.1/495
ESO 464-G016	$84.8^{+17.3}_{-15.6}$	$1.88^{+0.24}_{-0.22}$	67.9/76	$83.9^{+18.9}_{-17.5}$	$1.71^{+0.29}_{-0.27}$	67.0/75
NGC 7130	$221.8^{+42.4}_{-29.4}$	$1.50^{+0.19}_{-0.10l}$	61.3/83	$399.0^{+358.0}_{-137.2}$	$1.45^{+0.15}_{-0.05l}$	67.9/82
NGC 7212	$126.9^{+31.4}_{-24.5}$	$1.92^{+0.16}_{-0.17}$	129.0/121	$155.5^{+31.4}_{-27.0}$	$1.77^{+0.10}_{-0.11}$	123.4/120
NGC 7479	$363.6^{+58.0}_{-50.3}$	$1.83^{+0.09}_{-0.09}$	200.6/171*	$542.5^{+411.3}_{-209.2}$	$1.79^{+0.13}_{-0.20}$	206.8/170*
NGC 7582	$525.6^{+231.8}_{-130.7}$	$2.00^{+0.05}_{-0.04}$	340.7/320	$174.2^{+26.8}_{-21.0}$	$1.90^{+0.05}_{-0.05}$	353.6 /319

Table 3

Best fit properties for the 35 candidate CT-AGN analyzed in this work, using either MYTorus or borus02 in the MYTorus configuration (covering factor $f_c=0.5$, observing angle $\theta_{\text{Obs}}=87^\circ$). $N_{\text{H},z}$ is the AGN line-of-sight column density, in units of 10^{22} cm^{-2} ; Γ is the power law photon index. In NGC 4102, leaving $N_{\text{H},z,2-10}$ free to vary with respect to $N_{\text{H},z,\text{NuS}}$ leads to a significant improvement of the fit: the reported value is the *NuSTAR* one. textbfSources flagged with ^N are objects where we fitted the *NuSTAR* data alone. Parameters fixed to a given value are flagged with ^f. 90% confidence errors flagged with ^l and ^u indicate that the value is pegged at either the lower ($\Gamma=1.4$ in both MYTorus and borus02) or the upper ($N_{\text{H},z}=10^{25} \text{ cm}^{-2}$ in MYTorus) boundary of the parameter in the MYTorus model. For these sources, the reported values should therefore be treated as lower limits on the actual 90% confidence uncertainties. Given their low quality, in NGC 7479 the XMM-*Newton* and *NuSTAR* spectra are fitted using Cstat, rather than χ^2 . The *Swift*-BAT data are instead already background subtracted and are therefore fitted using the χ^2 statistic. The best-fit statistic values we report for NGC 7479, flagged with *, are therefore the sum of the two.

As a preliminary caveat, we point out that the whole analysis reported in this Section is based on single-epoch *NuSTAR* observation: this represents a partial limitation to our approach, since it has been shown (see, e.g., Baloković et al. 2018), that the analysis of multi-epoch *NuSTAR* observations allows one to place stronger constraints on the covering factor, simultaneously reducing potential degeneracies between parameters. Nonetheless, this work represents, as of today, the most complete analysis of single-epoch *NuSTAR* spectra of nearby, heavily obscured AGNs.

In using **borus02** with f_c as a free parameter, we followed the approach adopted by Baloković et al. (2018) when fitting single-epoch *NuSTAR* observations. Therefore, for each object we performed a set of 36 fits, in each of which we kept $N_{\text{H,tor}}$ fixed: in each iteration, we increased the $\log(N_{\text{H,tor}})$ value by 0.1, starting from $\log(N_{\text{H,tor}})=22$ and stopping at $\log(N_{\text{H,tor}})=25.5$, i.e., the lower and upper boundaries of the parameter in **borus02**. We then assumed as best-fit $N_{\text{H,tor}}$ the one corresponding to the minimum χ^2 fit. Furthermore, we also report in Appendices B and C the confidence contours of f_c against the line-of-sight column density and $\log(N_{\text{H,tor}})$, respectively. As can be seen, we find no evidence of degeneracy between f_c and either of the two column densities, and in the vast majority of the cases we are able to reliably constrain all three parameters.

To avoid complications in the spectral fitting caused by potential degeneracies between the torus covering factor, f_c , the torus average column density, $N_{\text{H,tor}}$, and the angle between the observer and the torus axis, θ_{Obs} , we also decided to fix this last parameter to its upper boundary, $\theta_{\text{Obs}}=87^\circ$, i.e., we assume that the torus is observed almost edge-on. Notably, this same approach was adopted in Brightman et al. (2015), and allows one to explore all the possible covering factor solutions.

We report the best-fit spectra obtained using **borus02** having f_c as a free parameter in Appendix A, and the corresponding best-fit parameters in Table 4: as can be seen, RBS 1037 is the only source in our sample for which f_c is completely unconstrained. This is not an unexpected result, since RBS 1037 is one of the two unobscured AGNs in our sample. Notably, we find a similar result for the other unobscured AGN in our sample, MCG-01-30-041, for which we obtain a f_c best-fit value, but with large uncertainties ($f_c=0.62^{+0.28}_{-0.52l}$). We also find that NGC 424 and NGC 1068 are best-fitted with two reprocessed components, having same covering factor but different $N_{\text{H,tor}}$: notably, for both sources it has already been proposed in the literature either a reprocessing-dominated scenario (for NGC 424, see Baloković et al. 2014) or a multi-reprocessed component scenario (for NGC 1068, see Bauer et al. 2015).

We also point out that NGC 6240 is a well known dual AGN (see, e.g. Puccetti et al. 2016): in our analysis we use XMM-*Newton* and *NuSTAR* data for this source, and we therefore do not resolve the two nuclei, thus implying that our measurement of f_c for NGC 6240 should be treated as an average of f_c for the two nuclei. Notably, our best-fit parameters are in excellent agreement with those obtained by Puccetti et al. (2016) fitting the combined *Chandra*, *NuSTAR* and XMM-*Newton* spectrum. Furthermore, to test the reliability of our assumption, we

simulate two different XMM-*Newton*+*NuSTAR* spectra of NGC 6240, using the best-fit parameters of the two cores, as observed with *Chandra* and reported in Puccetti et al. (2016). In one simulation, we fix the covering factor of the Southern core (three times more luminous than the Northern one) to $f_{c,S}=1$, and that of the Northern core to $f_{c,N}=0.11$; in the second, we do the opposite (i.e., $f_{c,S}=0.11$ and $f_{c,N}=1$). In both simulations, we fix the average torus column density to $\log(N_{\text{H,tor}})=24.2$, i.e., the best-fit value we obtain in our analysis. We then fit the simulated spectra with a single- f_c model: we find that in both cases the spectra are best-fitted by a model having $f_c\sim 0.5-0.6\pm 0.1$. This test suggests that the f_c measurement we obtain for NGC 6240 can be treated as the average of the covering factors of the two nuclei: since for NGC 6240 we measure a covering factor $f_c=0.75^{+0.25}_{-0.24}$, it is therefore likely that both AGNs have large covering factors.

To further investigate the relation between f_c and both $N_{\text{H,z,l.o.s.}}$ and $N_{\text{H,tor}}$, we divide the 33 obscured AGNs in our sample in three different classes, based on their covering factor best-fit value and 90% confidence uncertainties:

1. High- f_c sources (red circles in Figure 3): objects having 90% confidence lower boundary >0.55 . 12 sources belong to this group.
2. Low- f_c sources (blue squares): objects having 90% confidence upper boundary <0.45 . 8 sources belong to this group.
3. Undefined- f_c sources (black stars): objects which do not belong to any of the two previous classes, mostly because of their large uncertainties on f_c . 13 sources belong to this group.

In Figure 3, left panel, we show the covering factor as a function of the line-of-sight column density: no clear trend can be immediately identified, especially around and above the Compton thick regime, where we observe both low- and high- f_c sources. Particularly, it is worth noting that all low- f_c objects have $\log(N_{\text{H,z,l.o.s.}})\geq 23.9$. However, as shown in Figure 3, central panel, all eight low- f_c sources have best-fit $\log(N_{\text{H,tor}})<24.1$, i.e., the average column density of the torus is not Compton thick in all sources but NGC 4945, where $N_{\text{H,tor}}$ is just above the CT-threshold. 8 out of 11 high- f_c sources (NGC 1068 is not included in this computation, since it has two different best-fit $N_{\text{H,tor}}$) have instead $\log(N_{\text{H,tor}})>24$, i.e., their obscuring torus is on average Compton thick.

We parameterize the difference between the torus average column density and the line-of sight column density with

$$\Delta N_{\text{H}} = |\log(N_{\text{H,tor}}) - \log(N_{\text{H,z,l.o.s.}})|. \quad (1)$$

We find that in the low- f_c sample the offset between the two column densities is large, being almost one order of magnitude ($\langle \Delta N_{\text{H,low-}f_c} \rangle = 0.82$, with standard deviation $\sigma=0.25$). In all eight sources, the average column density is smaller than the line-of-sight column density. Consequently, the low covering factor values measured in these objects can be linked to a ‘‘patchy torus’’ scenario, where the accreting SMBH is observed through an over-dense (with respect to the overall gas distribution) obscuring region.

On the basis of this result, the eight low- f_c objects can be promising candidates for long-term monitoring campaigns, with the aim of detecting significant flux and $N_{\text{H},z,1.o.s.}$ variability. In fact, in a patchy torus the line-of-sight obscuration is caused by an over-dense, Compton-thick cloud located in a less-dense, Compton-thin environment. In such a scenario, a monitoring campaign can allow one to observe a significant flux and/or line-of-sight column density variation (see, e.g., the case of NGC 1365 in Risaliti et al. 2005). Notably, one of these eight sources, NGC 4945, is already known to show strong >10 keV variability (see Section 6.2 for a more detailed discussion).

While all the low- f_c sources have best-fit $\log(N_{\text{H},\text{tor}}) < 24.1$, eight out of 11 high- f_c sources (i.e., 73% of the high- f_c subsample) have best-fit $\log(N_{\text{H},\text{tor}}) > 24$. Interestingly, two out of the three objects with high f_c and $\log(N_{\text{H},\text{tor}}) < 24$ are among the least obscured sources in our sample, namely 2MASXJ10523297+1036205 and MRK 477, thus suggesting a tighter correlation between $N_{\text{H},\text{tor}}$ and $N_{\text{H},z,1.o.s.}$ than the one observed in the low- f_c subsample. In fact, the average offset between the two column densities is $\langle \Delta N_{\text{H},\text{high-}f_c} \rangle = 0.53$, with standard deviation $\sigma = 0.20$.

In conclusion, we find potential evidence of correlation between the torus covering factor and the difference between the average torus column density and the line-of-sight column density, supporting a scenario where sources with low f_c are more likely to have a patchy torus, while sources with high f_c are more likely to be obscured by a more uniform distribution of gas.

6.1. Effects on $N_{\text{H},z,1.o.s.}$ and Γ with respect to the MYTorus configuration

In 27 out of 35 sources (77.1% of the whole sample) we find that leaving f_c free to vary does not affect significantly the measurement of the line-of-sight column density, i.e., the measurement of $N_{\text{H},z,1.o.s.}$ with **borus02** in the free- f_c configuration is consistent, within the 90% confidence uncertainties, with the one obtained using **MYTorus**.

Six out of the eight sources for which instead we find a significant disagreement between the two $N_{\text{H},z,1.o.s.}$ measurements show a significant improvement in the fit statistics ($\Delta\chi^2 = [8.5-35.3]$): we flag these sources with B in Table 4, and we assume that for these objects the measurements obtained with **borus02** should be treated as the best-fit solutions. This is particularly interesting for three of these six objects, namely MCG+08-03-018, ESO 201-IG004 and CGCG 420-15, which were found to have $\log(N_{\text{H},z,1.o.s.}) < 24$ using **MYTorus** and are instead re-classified as CT-AGNs using **borus02**, although only CGCG 420-15 has $\log(N_{\text{H},z,1.o.s.}) > 24$ at a $>3\sigma$ confidence level. Based on these new measurements, we find that 19 out of 35 candidate CT-AGNs (i.e., 54% of the sources in our sample) are confirmed CT-AGNs, while other three sources (IGR J14175-4641, NGC 5728 and ESO 464-G016) have $\log(N_{\text{H},z,1.o.s.}) < 24$ but their 90% confidence upper uncertainty lie above the CT threshold. In none of the eight sources with a significant discrepancy in the $N_{\text{H},z,1.o.s.}$ measurement the difference in line-of-sight column density can be explained exclusively by a discrepancy in the Γ measurement.

Finally, there is a general excellent consistency in the photon indices measurements, independently from the geometrical configuration assumed in **borus02**: in fact, 32 out of 35 sources (91.4% of the whole sample) have Γ in agreement within the 90% confidence uncertainty. In one of the remaining three sources, NGC 4945, the disagreement is actually fairly small, being $\Delta\Gamma/\Gamma_{\text{min}} = 0.06$, where Γ_{min} is the smallest of the two photon index measurements. The remaining two objects (NGC 1194 and CGCG 420-15) also have different $N_{\text{H},z,1.o.s.}$, and in both cases the fit is significantly improved ($\Delta\chi^2 = 10.3$ and $\Delta\chi^2 = 34.1$, respectively) in the fit where f_c is left free to vary.

6.2. Comparison with previous results

NGC 4945 is one of the sources in our sample for which several measurements of the covering factor are reported in literature. Particularly, several works (Madejski et al. 2000; Done et al. 2003; Yaqoob 2012; Puccetti et al. 2014) explained the significant variability observed in NGC 4945 above >10 keV, as well as the source weak reprocessed component, as two indicators of a low- f_c scenario for this object. However, Brightman et al. (2015), using the **BNTorus** model (Brightman & Nandra 2011) and its modified version with $f_c = 1$, **isphere**, found a high covering factor for NGC 4945, even consistent with $f_c = 1$. However, as pointed out by Liu & Li (2015), the **BNTorus** presents some issues in properly treating the AGN reprocessed component, therefore potentially leading to unreliable f_c measurements. The existence of this issue was then confirmed in Baloković et al. (2018), and properly taken into account when developing **borus02**.

In our analysis with **borus02** we find that the best-fit covering factor is pegged at the lower limit of the model, $f_c = 0.10_{-0.00}^{+0.12}$, in excellent agreement with the previous results reported in the literature. In Figure 4, left panel, we show how both f_c and the best-fit χ^2 vary as a function of the torus average covering factor: for $\log(N_{\text{H},\text{tor}}) \leq 24.1$ a low- f_c solution is preferred, the model best-fit χ^2 regularly decreasing since reaching a minimum at $\log N_{\text{H},\text{tor}} = 24.1$, where the best-fit statistic is $\chi_\nu = \chi^2/\text{d.o.f.} = 1404.1/1399 = 1.00$. At $\log N_{\text{H},\text{tor}} \geq 24.2$ we instead enter in the high- f_c solution regime, which has a significantly worse best-fit statistics: in this regime, we find a local χ^2 minimum at $\log N_{\text{H},\text{tor}} = 24.5$, where $f_c = 0.78_{-0.09}^{+0.13}$. However, while this potential high- f_c solution has a reasonable reduced χ^2 , $\chi_\nu = \chi^2/\text{d.o.f.} = 1433.6/1399 = 1.03$, the difference in χ^2 between the two solutions, $\Delta\chi^2 = 29.5$, suggests that a low- f_c solution is favored by our data.

Since NGC 4945 is known to be variable in intrinsic luminosity, and therefore the covering factor measurement is partially dependent on the observation used for the analysis, in our analysis we fitted the *NuSTAR* data alone, following the approach adopted by Brightman et al. (2015). Nonetheless, even multi-epoch studies with **borus02** (Baloković et al. 2019 in prep.) find a low- f_c solution ($f_c = 0.3 \pm 0.1$). In conclusion, our analysis favors a low- f_c solution for NGC 4945, in agreement with several other works. This result also confirms that the issue in **BNTorus** reported by Liu & Li (2015), i.e., the tendency to overestimate the strength of the reprocessed component in an edge-on configuration, has been

Source	$N_{\text{H},z, \text{l.o.s.}}$ 10^{22} cm^{-2}	Γ	$\log(N_{\text{H},\text{tor}})$	f_c	$\log(L_{2-10\text{keV}})$	χ^2/DOF
NGC 424	$265.1^{+44.4}_{-35.8}$	$1.81^{+0.07}_{-0.05}$	23.3, 24.3	$0.40^{+0.08}_{-0.08}$	$42.74^{+0.02}_{-0.02}$	398.6/335
MCG+08-03-018 ^B	$107.3^{+24.4}_{-22.2}$	$2.17^{+0.26}_{-0.19}$	23.1	$0.67^{+0.33u}_{-0.27}$	$43.27^{+0.16}_{-0.26}$	150.9/148
NGC 1068 ^N	1000 ^f	$2.15^{+0.04}_{-0.05}$	23.1, 24.7	$0.91^{+0.08}_{-0.05}$	$42.38^{+0.02}_{-0.02}$	574.0/551
NGC 1194 ^B	$246.6^{+40.6}_{-8.3}$	$1.86^{+0.09}_{-0.05}$	23.8	$0.10^{+0.09}_{-0.00l}$	$43.61^{+0.07}_{-0.09}$	262.6/243
NGC 1229	$35.2^{+9.6}_{-7.3}$	$1.57^{+0.14}_{-0.16}$	24.2	$1.00^{+0.00u}_{-0.32}$	$42.83^{+0.22}_{-0.47}$	91.8/95
ESO 116-G018	$313.0^{+43.0}_{-14.0}$	$1.59^{+0.22}_{-0.19l}$	23.5	$0.12^{+0.16}_{-0.02l}$	$43.30^{+0.47}_{-0.42}$	189.0/209
NGC 1358	$255.0^{+14.0}_{-10.0}$	$1.60^{+0.10}_{-0.07}$	23.8	$0.14^{+0.05}_{-0.04l}$	$43.40^{+0.21}_{-0.33}$	231.0/238
ESO 201-IG004 ^B	$133.8^{+35.7}_{-32.4}$	$1.69^{+0.21}_{-0.21}$	23.2	$0.40^{+0.27}_{-0.16}$	$43.53^{+0.21}_{-0.42}$	96.2/83
2MASXJ03561995-6251391	$84.3^{+10.7}_{-11.4}$	$1.99^{+0.20}_{-0.26}$	24.5	$0.51^{+0.31}_{-0.41l}$	$44.55^{+0.16}_{-0.26}$	132.2/137
CGCG 420-15 ^B	$150.0^{+24.8}_{-21.9}$	$1.92^{+0.14}_{-0.13}$	23.4	$0.28^{+0.11}_{-0.08}$	$41.83^{+0.09}_{-0.12}$	225.9/218
MRK 3	$79.5^{+2.9}_{-1.9}$	$1.68^{+0.03}_{-0.02}$	22.7	$0.30^{+0.07}_{-0.08}$	$44.04^{+0.06}_{-0.07}$	1120.1/1097
ESO 005-G004	$248.1^{+85.9}_{-61.7}$	$1.47^{+0.12}_{-0.07l}$	23.7	$1.00^{+0.00u}_{-0.56}$	$41.87^{+0.27}_{-0.89}$	86.1/71
MCG+06-16-028	$82.2^{+10.9}_{-10.9}$	$1.83^{+0.15}_{-0.15}$	24.5	$1.00^{+0.00u}_{-0.17}$	$42.84^{+0.18}_{-0.31}$	69.4/86
2MASXJ09235371-3141305	$63.2^{+8.9}_{-6.1}$	$2.01^{+0.10}_{-0.13}$	24.3	$1.00^{+0.00u}_{-0.33}$	$43.57^{+0.41}_{-0.62}$	178.5/144
NGC 3079 ^B	$150.5^{+19.1}_{-9.0}$	$1.93^{+0.06}_{-0.10}$	24.5	$0.98^{+0.02u}_{-0.29}$	$41.83^{+0.03}_{-0.03}$	194.6/181
NGC 3393	$257.8^{+132.3}_{-86.7}$	$1.72^{+0.22}_{-0.13}$	24.2	$0.60^{+0.40u}_{-0.47}$	$42.75^{+0.07}_{-0.09}$	55.3/91
2MASXJ10523297+1036205	$7.5^{+2.3}_{-2.1}$	$1.51^{+0.04}_{-0.04}$	22.7	$1.00^{+0.00u}_{-0.12}$	$43.90^{+0.09}_{-0.11}$	521.1/513
RBS 1037	<0.1	$1.85^{+0.04}_{-0.07}$	23.6	–	$42.71^{+0.02}_{-0.02}$	317.2/312
MCG-01-30-041	<1.7	$1.85^{+0.09}_{-0.09}$	24.8	$0.62^{+0.30}_{-0.52l}$	$43.90^{+0.03}_{-0.04}$	219.9/224
NGC 4102	$62.3^{+8.7}_{-7.7}$	$1.75^{+0.09}_{-0.11}$	24.3	$0.77^{+0.23u}_{-0.27}$	$41.29^{+0.06}_{-0.06}$	201.3/190
B2 1204+34	$5.3^{+0.8}_{-1.0}$	$1.86^{+0.05}_{-0.13}$	24.4	$0.90^{+0.10u}_{-0.38}$	$43.65^{+0.13}_{-0.19}$	214.5/247
NGC 4945 ^N	$397.2^{+15.2}_{-15.2}$	$1.95^{+0.06}_{-0.06}$	24.1	$0.10^{+0.12}_{-0.00l}$	$42.33^{+0.04}_{-0.04}$	1404.1/1398
NGC 5100	$20.4^{+4.3}_{-2.7}$	$1.57^{+0.11}_{-0.07}$	23.3	$1.00^{+0.00u}_{-0.46}$	$42.99^{+0.23}_{-0.54}$	189.7/196
IGR J14175-4641	$85.9^{+24.9}_{-18.6}$	$1.70^{+0.21}_{-0.19}$	23.2	$0.19^{+0.25}_{-0.09l}$	$43.96^{+0.34}_{-0.73}$	83.6/79
NGC 5643	$269.4^{+187.5}_{-65.0}$	$1.55^{+0.13}_{-0.15}$	23.6	$1.00^{+0.00u}_{-0.37}$	$41.42^{+0.06}_{-0.06}$	150.0/137
MRK 477	$16.8^{+3.7}_{-3.5}$	$1.60^{+0.06}_{-0.06}$	23.7	$1.00^{+0.00u}_{-0.14}$	$43.09^{+0.04}_{-0.05}$	223.0/223
NGC 5728 ^B	$96.8^{+5.2}_{-3.3}$	$1.81^{+0.07}_{-0.04}$	24.3	$1.00^{+0.00u}_{-0.03}$	$42.74^{+0.09}_{-0.12}$	327.1/328
CGCG 164-019	$137.1^{+57.1}_{-44.6}$	$1.79^{+0.36}_{-0.32}$	23.1	$0.40^{+0.40}_{-0.20}$	$42.43^{+0.17}_{-0.28}$	59.3/57
NGC 6232	$62.6^{+13.2}_{-23.5}$	1.40 ^f	25.1	$1.00^{+0.00u}_{-0.53}$	$41.89^{+0.18}_{-0.30}$	32.8/33
NGC 6240	$110.4^{+10.4}_{-8.3}$	$1.75^{+0.03}_{-0.04}$	24.2	$0.75^{+0.25u}_{-0.24}$	$43.58^{+0.02}_{-0.02}$	518.7/495
ESO 464-G016	$85.5^{+25.3}_{-17.2}$	$1.67^{+0.29}_{-0.27}$	22.8	$0.15^{+0.05}_{-0.05l}$	$43.17^{+0.70}_{-0.98}$	67.2/74
NGC 7130	$343.1^{+656.9}_{-126.3}$	1.40 ^f	24.1	$1.00^{+0.00u}_{-0.41}$	$42.30^{+0.06}_{-0.06}$	66.0/82
NGC 7212	$194.4^{+48.8}_{-42.7}$	$1.99^{+0.30}_{-0.22}$	23.6	$0.26^{+0.23}_{-0.16l}$	$43.63^{+0.08}_{-0.09}$	120.6/120
NGC 7479	$132.4^{+23.8}_{-27.7}$	$1.64^{+0.14}_{-0.19}$	24.8	$1.00^{+0.00u}_{-0.06}$	$42.02^{+0.15}_{-0.19}$	167.2/170
NGC 7582	1000.0 ^f	$1.96^{+0.03}_{-0.05}$	24.2	$1.00^{+0.00u}_{-0.17}$	$42.53^{+0.07}_{-0.08}$	316.6/317

Table 4

Best fit properties for the 35 candidate CT-AGNs analyzed in this work, using *borus02* allowing the covering factor, f_c , to vary. $N_{\text{H},z}$ is the torus line-of-sight column density, in units of 10^{22} cm^{-2} ; Γ is the power law photon index. $\log(N_{\text{H},\text{tor}})$ is the logarithm of the torus overall column density (in units of cm^{-2}), i.e., the $N_{\text{H},\text{tor}}$ value for which we obtain the smallest χ_ν value (see the text for more details), f_c is the torus covering factor and $\log(L_{2-10\text{keV}}$ is the logarithm of the intrinsic, absorption corrected 2–10 keV luminosity (in units of erg s^{-1}). Sources flagged with ^B are objects for which the $N_{\text{H},z}$ measurement differs significantly from the one obtained using *borus02* in the MYTorus geometrical configuration, and for which the χ^2 of the fit is significantly improved (see Section 6.1), while sources flagged with ^N are objects where we fitted the *NuSTAR* data alone. Parameters fixed to a given value are flagged with ^f. 90% confidence errors flagged with *l* and *u* indicate that the value is pegged at either the lower ($\Gamma=1.4$; $f_c=0.1$) or the upper ($f_c=0.91$) boundary of a given parameter. For these sources, the reported values should therefore be treated as lower limits on the actual 90% confidence uncertainties. Finally, f_c is unconstrained in RBS 1037, one of the two unobscured AGN in our sample.

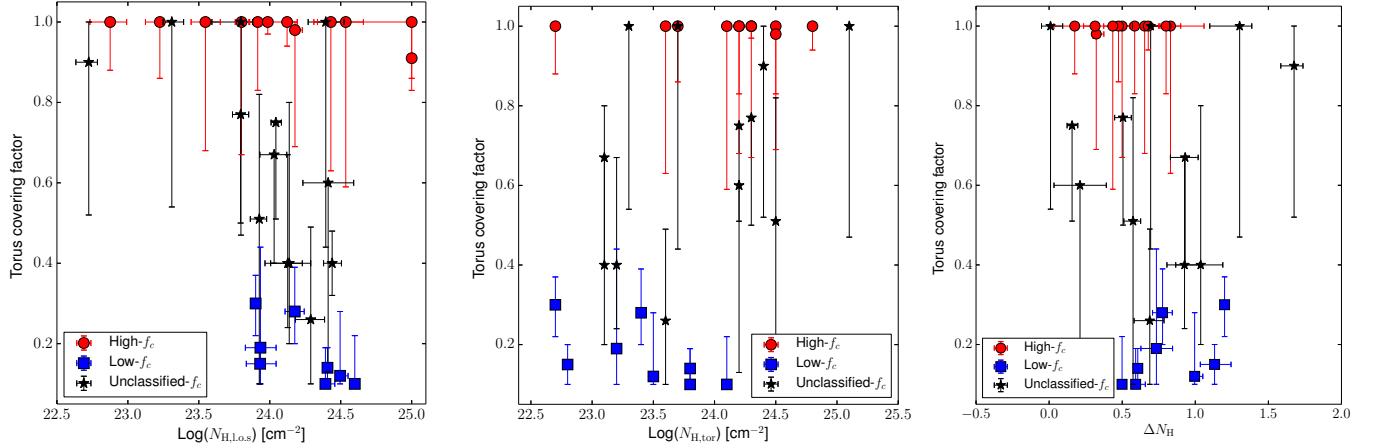


Figure 3. Torus covering factor as a function of the line-of-sight column density ($N_{\text{H,z,l.o.s.}}$, left), the torus average column density ($N_{\text{H,tor}}$, center) and the difference between the logarithms of the two quantities (ΔN_{H}) for the sources in our sample having $N_{\text{H,z,l.o.s.}} > 10^{22} \text{ cm}^{-2}$. Since NGC 424 and NGC 1068 are best fitted with two reprocessed components, having different $N_{\text{H,tor}}$, we do not report them in the central and right panel. Sources with covering factor 90% confidence lower boundary > 0.55 are plotted as red circles, sources with with covering factor 90% confidence upper boundary < 0.45 are plotted as blue squares, and sources not belonging to either of the other two classes are plotted as black stars.

properly taken into account in *borus02*.

Another source, NGC 3079, was also part of the sample studied by Brightman et al. (2015). One of their *BNTorus* best-fit solutions implies a small covering factor, $f_c=0.18^{+0.16}_{-0.03}$, but they also reported a potential second solution with $f_c>0.90$, and fitting the data with the *sphere* model, i.e., assuming $f_c=1$, also led to a slightly improved best-fit statistics, from $\chi^2_\nu=1.33$ to $\chi^2_\nu=1.31$. In our work, we find that the best-fit covering factor, corresponding to a torus average column density $\log(N_{\text{H,tor}})=24.5$, is $f_c=0.90^{+0.01u}_{-0.21}$, in good agreement with the second of the solutions reported in Brightman et al. (2015); the reduced χ^2 of this solution is $\chi^2_\nu=194.2/181=1.07$. However, as we show in Figure 4, right panel, assuming a slightly lower average torus column density, $\log(N_{\text{H,tor}})=24.3$, leads to a small covering factor solution, $f_c=0.15^{+0.05}_{-0.02l}$; the reduced χ^2 of this second solution is $\chi^2_\nu=201.8/181=1.11$, with a χ^2 difference $\Delta\chi^2=7.6$. Consequently, we find that a high covering factor solution for NGC 3079 is favored by our data, but a small covering factor cannot be ruled out at a $>3\sigma$ level.

Finally, the covering factor of NGC 7582 was recently measured by Baloković et al. (2018), using *borus02* and fitting the *NuSTAR* data alone. As expected, since they used the same model we used in our analysis, their results are in excellent agreement with ours: they find a best-fit covering factor $f_c=0.9$ and a torus average column density $\log(N_{\text{H,tor}})=24.5$, while our best-fit result, obtained combining *NuSTAR* and *Swift*-XRT data, is $f_c=0.91^{+0.00u}_{-0.08}$ for $\log(N_{\text{H,tor}})=24.2$. We point out that even assuming $\log(N_{\text{H,tor}})=24.5$, as reported in Baloković et al. (2018), leads to a high covering factor, $f_c=0.9$, although with a significantly worse best-fit χ^2 .

Notably, the torus covering factor can be measured also using dusty torus models based on the mid-infrared (mIR; $\sim 7.5\text{--}13.5\ \mu\text{m}$) spectral energy distribution (SED) fitting. Most of these models assume a clumpy distribution of the obscuring material (see, e.g., Rowan-Robinson 1995; Nenkova et al. 2002, 2008; Hönig & Kishimoto 2010; García-González et al. 2017), thus differing from both *MYTorus* and *borus02*, where the obscuring material is assumed to be uniformly distributed.

Alonso-Herrero et al. (2011) used the *CLUMPY* model Nenkova et al. (2008) to fit the infrared SED and measure the torus properties of a sample of 13 nearby Seyfert galaxies, among which there are also two objects we study in this work, NGC 1068 and NGC 7582. We find that for both sources there is a remarkable agreement between the f_c value measured from the X-ray spectral fitting and the one inferred from the IR SED-fitting: more in detail, NGC 1068 has $f_{c,X}=0.40\pm 0.01$ and $f_{c,IR}=0.30^{+0.11}_{-0.08}$, while NGC 7582 has $f_{c,X}=0.91^{+0.00u}_{-0.08}$ and $f_{c,IR}=0.83^{+0.06}_{-0.14}$.

6.3. Covering factor trend with 2-10 keV luminosity

In Figure 5, left panel, we plot the torus covering factor as a function of the de-absorbed 2–10 keV luminosity for the 31 objects in our sample with $\log(N_{\text{H,z}})\geq 23$. As in Figure 3, the sources are divided in high- f_c objects (red circles), low- f_c objects (blue squares) and undefined- f_c objects (black stars). Since no clear trend between

the two quantities is immediately visible in our sample, we measure the difference in average $L_{2-10\text{keV}}$ between the high- and the low- f_c sample. The eleven high- f_c sources with $\log(N_{\text{H,z}})\geq 23$ have average 2–10 keV luminosity $\langle\log(L_{2-10\text{keV,H-}f_c})\rangle=42.84$, with standard deviation $\sigma_{\log(L_{2-10}),\text{Hf}_c}=0.57$. The eight low- f_c sources with $\log(N_{\text{H,z}})\geq 23$, instead, have $\langle\log(L_{2-10\text{keV,L-}f_c})\rangle=43.58$, with $\sigma_{\log(L_{2-10}),\text{Lf}_c}=0.72$. When we perform a KS-test, we find that the hypothesis that the two $L_{2-10\text{keV}}$ samples are drawn from the same population can be rejected at the $\sim 2.5\sigma$ level (p-value=0.018), a (marginal) evidence of the existence of different luminosity trends in high- and low- f_c sources.

While the overall distribution has large dispersion and only a marginal visible trend, when we compute the weighted average of f_c in five different bins we find significant evidence of anti-correlation in our sample: as can be seen in Figure 5, right panel, at $\log(L_{2-10\text{keV}})<43$ the average covering factor (green diamonds) value is $f_c\sim 0.6\text{--}0.8$, while at $\log(L_{2-10\text{keV}})>43$ the average covering factor value drops to $f_c\sim 0.2$. At $\log(L_{2-10\text{keV}})>42.5$, these results are in reasonable agreement with the trend reported in Brightman et al. (2015) using a sample of 8 CT-AGNs fitted with *BNTorus*, and plotted as a black dotted line. At lower luminosities, instead, we find an average covering factor $\langle f_c \rangle\sim 0.7$, in significant disagreement with the expected $f_c\sim 1$ reported by Brightman et al. (2015). We remind that our results are obtained with a sample 3.5 times larger than the Brightman et al. (2015) one, and that we made use of the *borus02* model, rather than the *BNTorus* one.

In Figure 5, right panel, we also show the fraction of obscured AGN, $f_{\text{obs}}=N_{\text{obs}}/N_{\text{tot}}$, as a function of $L_{2-10\text{keV}}$, computed by Burlon et al. (2011, black solid line) and Vasudevan et al. (2013, magenta dashed line). The Burlon et al. (2011) obscured fraction has been computed dividing the 15–55 keV luminosity function (XLF) of the obscured AGN by the overall XLF, while the Vasudevan et al. (2013) one is derived directly counting the number of obscured AGN with respect to the whole population, in each bin of luminosity. As can be seen, the two curves show a fair agreement over the whole luminosity range, peaking at $\log(L_{2-10\text{keV}})\sim 42.5\text{--}43$ and declining significantly both at lower and at higher luminosities. A trend similar to the one observed in these two works has also been recently observed by Ricci et al. (2017b), using a complete sample of 731 AGNs from the 70-month *Swift*-BAT catalog. The existence of a luminosity-dependent covering factor in CT-AGNs was also mentioned in Boorman et al. (2018), as a potential cause for the observed anti-correlation between the Fe K α equivalent width and the AGN bolometric luminosity.

Both curves have been computed from a sample of bright BAT-selected AGNs in the local Universe, and can therefore be compared with our results, since our sample has been selected in the same way. Furthermore, the f_c of a source is also an indicator of the probability to observe that source as obscured (the higher the covering factor, the higher the probability), therefore f_c and f_{obs} may in principle be directly compared. As for the anti-correlation between f_c and $L_{2-10\text{keV}}$, we find some tentative agreement between our weighted average data and the measured fractions of obscured AGNs, particu-

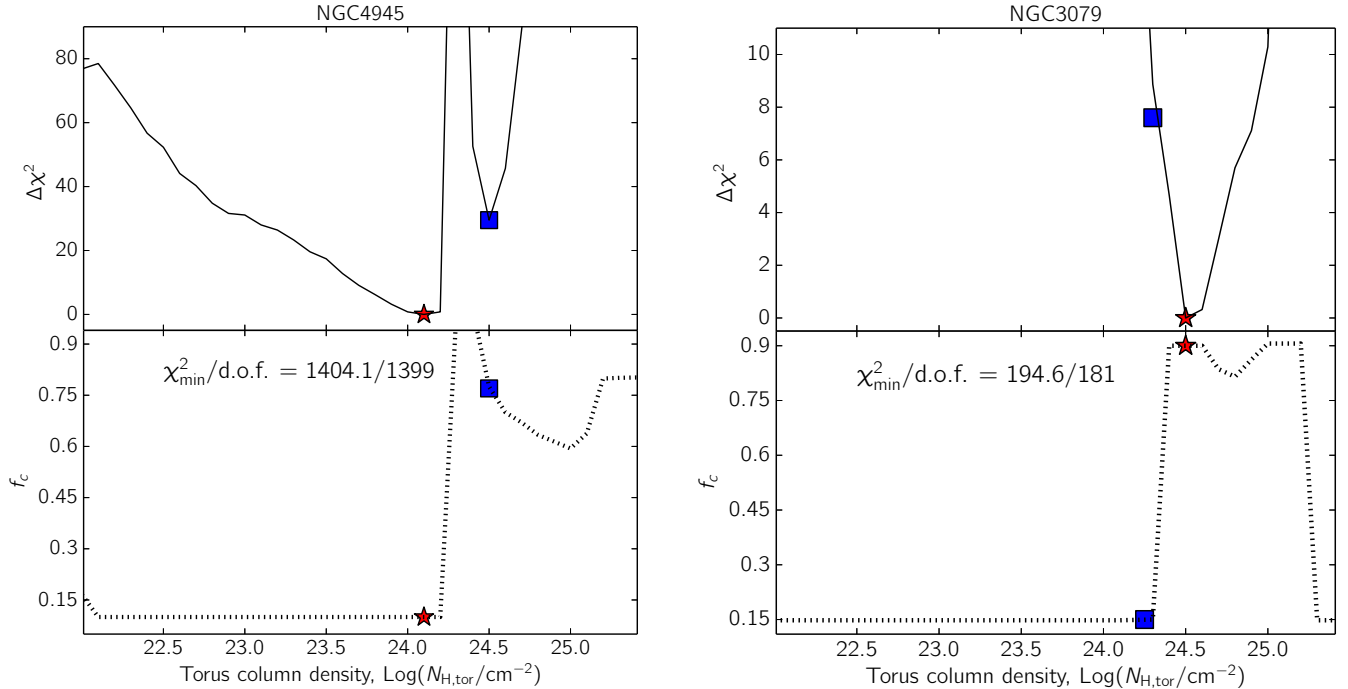


Figure 4. Estimate of the torus covering factor in NGC 4945 (left) and NGC 3079 (right). Top panel: difference between the best-fit, minimum χ^2 (χ^2_{\min}) and the χ^2 associated to $\log(N_{\text{H,tor}})$, as a function of the torus average column density. Bottom panel: torus covering factor as a function of the torus average column density. In both panels, we plot as a red star the combination of parameters associated to χ^2_{\min} , and as a blue square the potential alternative f_c solution we discuss in the text.

larly with the Vasudevan et al. (2013) one.

Finally, in Figure 5, right panel, we also plot the intrinsic fraction of CT-AGNs derived in two different works: the magenta circle is the measurement in the redshift range $0.04 < z < 1$ made by Lanzuisi et al. (2018), which computed the intrinsic CT fraction using the *Chandra COSMOS-Legacy* (Civano et al. 2016; Marchesi et al. 2016a) AGN sample; the orange square is instead the one derived by Ricci et al. (2015) using the 70-month BAT catalog and assuming a torus opening angle $\theta_{\text{OA}} = 60^\circ$. As can be seen, both measurements are in good agreement with both our result and the obscured AGN fractions measured by Burlon et al. (2011) and Vasudevan et al. (2013).

7. CONCLUSIONS

In this work, we analyzed the combined 2–100 keV spectra of 35 AGNs selected in the 100-month BAT catalog. These objects have been selected among those candidate CT sources in the 100-month BAT catalog having an archival *NuSTAR* observation. In this work, we used only single-epoch *NuSTAR* observations. 30 out of 35 sources were already analyzed in Marchesi et al. (2018) using *MYTorus*. We report the main results of our analysis.

1. Among the five sources not studied in M18, three (ESO 116-G018, NGC 1358 and NGC 7479) are confirmed to be CT-AGNs at a $>3\sigma$ level. A fourth

object, Mrk 3, is found to have best-fit line-of-sight column density $N_{\text{H,z}} = (7.8 \pm 0.1) \times 10^{23} \text{ cm}^{-2}$, slightly below the CT threshold: this source is known to be highly variable, having line-of-sight column density varying in the range $N_{\text{H,z}} = [0.75 - 0.94] \times 10^{24} \text{ cm}^{-2}$ in a timespan of seven months. Finally, we find that MCG-01-30-041, a candidate CT-AGN reported by Vasudevan et al. (2013), is in fact an unobscured AGN ($N_{\text{H,z}} < 10^{22} \text{ cm}^{-2}$). This discrepancy is likely caused by the low quality of the *Swift*-XRT and *Swift*-BAT data fitted by Vasudevan et al. (2013).

2. For all the 35 sources in our sample, we compared the best-fit line-of-sight column density obtained using *MYTorus* with those obtained using the new *borus02* with the same geometrical configuration of *MYTorus*, i.e., fixing the torus covering factor to $f_c = 0.5$. We find that there is a general excellent agreement between the $N_{\text{H,z}}$ value obtained using *borus02* and the one obtained using *MYTorus* (see Figure 2, left panel). While this trend is driven by the non-CT population, the weaker, albeit existent correlation observed in CT sources is not unexpected, given the increasing complexity in properly constrain the AGN spectral parameters in the CT-regime since above the CT threshold the $N_{\text{H,z}}$. Nonetheless, 11 out of 16 sources confirmed CT-AGNs have $N_{\text{H,z}}$ values in agreement at the 90% confidence level.

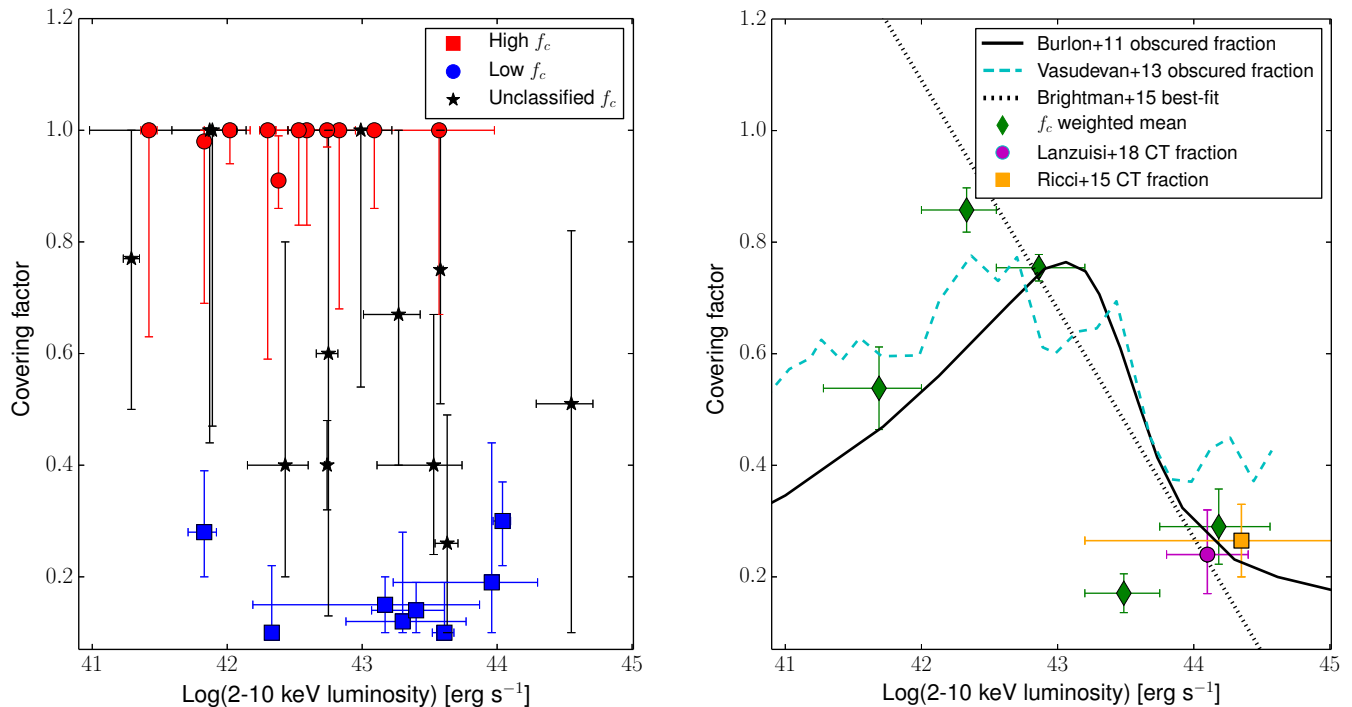


Figure 5. *Left:* torus covering factor, f_c , as a function of the intrinsic, absorption-corrected 2–10 keV luminosity for the 31 sources in our sample having $\log(N_{\text{H,z}}) \geq 23$. Objects with covering factor 90% confidence lower boundary > 0.55 are plotted as red circles, sources with with covering factor 90% confidence upper boundary < 0.45 are plotted as blue squares, and sources not belonging to either of the other two classes are plotted as black stars. *Right:* same as left, but this time plotting f_c in five different luminosity bins (green diamonds). The best-fit to the same relation computed by Brightman et al. (2015) for a sample of 8 CT-AGNs is plotted as black dotted line. Measurements of the obscured fraction of AGNs with respect to the total population as computed by Burlon et al. (2011, black solid line) and Vasudevan et al. (2013, cyan dashed line) in samples of BAT-selected AGNs in the nearby Universe are also plotted for comparison, together with the CT fraction measurements made by Lanzuisi et al. (2018, magenta circle) and Ricci et al. (2015, orange square)

3. We find an overall remarkable agreement between the photon indices obtained using `MYTorus` and those measured with `borus02` in the same geometrical configuration of `MYTorus` (see Figure 2, right panel). 29 out of 35 sources have Γ_{Borus} consistent with Γ_{MyT} within the 90% confidence uncertainty.
4. After validating `borus02` showing its excellent agreement with `MYTorus`, we used it to measure the torus covering factor and average column density for the 35 objects in our sample. We find 12 high- f_c sources, i.e., objects having 90% confidence lower boundary > 0.55 ; 8 low- f_c sources, i.e., objects having 90% confidence lower boundary < 0.45 ; and 15 undefined- f_c sources, i.e., objects do not belonging to either of the two groups.
5. We find a tentative evidence of different trends between f_c and the difference between the average torus column density and the line-of-sight column density: the offset is larger in low- f_c objects, where the average column density is always smaller than the line-of-sight column density, than in high- f_c objects. These results are consistent with a scenario where low- f_c AGNs are more likely to have a patchy torus, while high- f_c AGNs are more likely to be obscured by a more uniform distribution of gas.
6. In 6 out of 35 sources, leaving f_c to vary leads to a significant variation in the line-of-sight column density measurement, and a corresponding significant improvement in the best-fit χ^2 value. Interestingly, three of these objects (MCG+08-03-018, ESO 201-IG004 and CGCG 420-15), which were found to have $\log(N_{\text{H,z,l.o.s.}}) < 24$ using `MYTorus`, are now reclassified as CT-AGN on the basis of the `borus02` modelling. Overall, 19 out of 35 candidate CT-AGNs (54% of the sources in our sample) are confirmed CT-AGNs.
7. We find that our data favors a low- f_c solution for NGC 4945 ($f_c < 0.22$), in agreement with previous results based on the strength of the reprocessed component and the observed strong variability at energies > 10 keV.
8. We find potential evidence of an inverse trend between the torus covering factor and the AGN 2–10 keV luminosity (Figure 5, right panel), i.e.,

sources with higher f_c values have on average lower luminosities, although the f_c dispersion in sources in the same range of luminosity is large. Our results partially disagree, in the low-luminosity regime, with the findings of Brightman et al. (2015), since we observe a flattening in the anti-correlation at $\text{Log}(L_{2-10\text{keV}}) < 42.5$, while they observed a more regular trend, implying that the vast majority of CT-AGN should have $f_c \sim 1$ at $\text{Log}(L_{2-10\text{keV}}) < 42$. However, their analysis was performed using a sample of only 8 sources, while we have 31 objects with $\text{log}(N_{\text{H},z}) \geq 23$. The trend we observe needs however to be validated using a larger sample of sources, all observed with *NuSTAR* to properly constrain both

$N_{\text{H},z}$ and $L_{2-10\text{keV}}$.

ACKNOWLEDGEMENTS

We thank an anonymous referee for the useful comments, which helped in improving the paper.

S.M., M.A., and X.Z. acknowledge funding under NASA contract 80NSSC17K0635. Mi.Ba. acknowledges support from the Black Hole Initiative at Harvard University, which is funded by a grant from the John Templeton Foundation. This work made use of data supplied by the UK Swift Science Data Centre at the University of Leicester, as well as of the TOPCAT software (Taylor 2005) for the analysis of data tables.

APPENDIX

A. BORUS02 BEST-FIT SPECTRA

We report in Figures 6–11 the unfolded spectra and data-to-model ratios of all the 35 sources in our sample. The best-fit models are those obtained using *borus02* with the covering factor left free to vary: the best-fit parameters of these spectra are reported in Table 4.

B. CONFIDENCE CONTOURS OF THE TORUS COVERING FACTOR VERSUS THE LINE-OF-SIGHT COLUMN DENSITY

We report in Figures 12–17 the confidence contours of the covering factor, f_c , versus the line-of-sight column density, $N_{\text{H},z}$, for 32 sources out of the 35 in our sample. We do not report the contours of NGC 1068 and NGC 7582, where we fix the line-of-sight column density to $N_{\text{H},z} = 10^{25} \text{ cm}^{-2}$, and of RBS 1037, which is an unobscured AGN where f_c is unconstrained.

C. CONFIDENCE CONTOURS OF THE TORUS COVERING FACTOR VERSUS THE TORUS AVERAGE COLUMN DENSITY

We report in Figure 18–23 the confidence contours of the covering factor, f_c , versus the logarithm of the torus average density, $\text{Log}(N_{\text{H},\text{tor}})$, for 31 sources out of the 35 in our sample. We do not report the contours of NGC 424 and NGC 1068, which are best-fitted by a multi-reprocessed component and therefore have more than one best-fit $\text{Log}(N_{\text{H},\text{tor}})$ (see Table 4), and those of MCG-01-30-041 and RBS 1037, the two unobscured AGNs in our sample, because f_c and/or $\text{Log}(N_{\text{H},\text{tor}})$ are unconstrained.

REFERENCES

- Ajello, M., Greiner, J., Sato, G., et al. 2008, *ApJ*, 689, 666
Alonso-Herrero, A., Ramos Almeida, C., Mason, R., et al. 2011, *ApJ*, 736, 82
Anders, E. & Grevesse, N. 1989, *Geochim. Cosmochim. Acta*, 53, 197
Annular, A., Gandhi, P., Alexander, D. M., et al. 2015, *ApJ*, 815, 36
Arnaud, K. A. 1996, in *Astronomical Society of the Pacific Conference Series*, Vol. 101, *Astronomical Data Analysis Software and Systems V*, ed. G. H. Jacoby & J. Barnes, 17
Awaki, H., Terashima, Y., Higaki, Y., & Fukazawa, Y. 2009, *PASJ*, 61, S317
Baloković, M., Brightman, M., Harrison, F. A., et al. 2018, *ApJ*, 854, 42
Baloković, M., Comastri, A., Harrison, F. A., et al. 2014, *ApJ*, 794, 111
Bauer, F. E., Arévalo, P., Walton, D. J., et al. 2015, *ApJ*, 812, 116
Boorman, P. G., Gandhi, P., Baloković, M., et al. 2018, *MNRAS*, 477, 3775
Brightman, M., Baloković, M., Stern, D., et al. 2015, *ApJ*, 805, 41
Brightman, M. & Nandra, K. 2011, *MNRAS*, 413, 1206
Burlon, D., Ajello, M., Greiner, J., et al. 2011, *ApJ*, 728, 58
Burtscher, L., Meisenheimer, K., Tristram, K. R. W., et al. 2013, *A&A*, 558, A149
Cappi, M., Bassani, L., Comastri, A., et al. 1999, *A&A*, 344, 857
Civano, F., Marchesi, S., Comastri, A., et al. 2016, *ApJ*, 819, 62
Cusumano, G., La Parola, V., Segreto, A., et al. 2010, *A&A*, 524, A64
Done, C., Madejski, G. M., Życki, P. T., & Greenhill, L. J. 2003, *ApJ*, 588, 763
Eguchi, S., Ueda, Y., Awaki, H., et al. 2011, *ApJ*, 729, 31
Elitzur, M. & Shlosman, I. 2006, *ApJL*, 648, L101
Evans, P. A., Beardmore, A. P., Page, K. L., et al. 2009, *MNRAS*, 397, 1177
Farrah, D., Baloković, M., Stern, D., et al. 2016, *ApJ*, 831, 76
García-González, J., Alonso-Herrero, A., Hönig, S. F., et al. 2017, *MNRAS*, 470, 2578
Gilli, R., Comastri, A., & Hasinger, G. 2007, *A&A*, 463, 79
Guainazzi, M., Risaliti, G., Awaki, H., et al. 2016, *MNRAS*, 460, 1954
Harrison, F. A., Craig, W. W., Christensen, F. E., et al. 2013, *ApJ*, 770, 103
Hönig, S. F. & Beckert, T. 2007, *MNRAS*, 380, 1172
Hönig, S. F. & Kishimoto, M. 2010, *A&A*, 523, A27
Jaffe, W., Meisenheimer, K., Röttgering, H. J. A., et al. 2004, *Nature*, 429, 47
Kalberla, P. M. W., Burton, W. B., Hartmann, D., et al. 2005, *A&A*, 440, 775
Kawamuro, T., Ueda, Y., Tazaki, F., & Terashima, Y. 2013, *ApJ*, 770, 157
Koss, M. J., Assef, R., Baloković, M., et al. 2016, *ApJ*, 825, 85
Koss, M. J., Romero-Cañizales, C., Baronchelli, L., et al. 2015, *ApJ*, 807, 149
Lanzuisi, G., Civano, F., Marchesi, S., et al. 2018, *MNRAS*, 480, 2578
Lawrence, A. 1991, *MNRAS*, 252, 586
Liu, Y. & Li, X. 2015, *MNRAS*, 448, L53
Madejski, G., Życki, P., Done, C., et al. 2000, *ApJL*, 535, L87
Marchesi, S., Ajello, M., Comastri, A., et al. 2017, *ApJ*, 836, 116
Marchesi, S., Ajello, M., Marcotulli, L., et al. 2018, *ApJ*, 854, 49
Marchesi, S., Civano, F., Elvis, M., et al. 2016a, *ApJ*, 817, 34
Marchesi, S., Lanzuisi, G., Civano, F., et al. 2016b, *ApJ*, 830, 100
Masini, A., Comastri, A., Baloković, M., et al. 2016, *A&A*, 589, A59
Murphy, K. D. & Yaqoob, T. 2009, *MNRAS*, 397, 1549
Nenkova, M., Ivezić, Ž., & Elitzur, M. 2002, *ApJL*, 570, L9
Nenkova, M., Sirocky, M. M., Ivezić, Ž., & Elitzur, M. 2008, *ApJ*, 685, 147
Oh, K., Koss, M., Markwardt, C. B., et al. 2018, *ApJS*, 235, 4

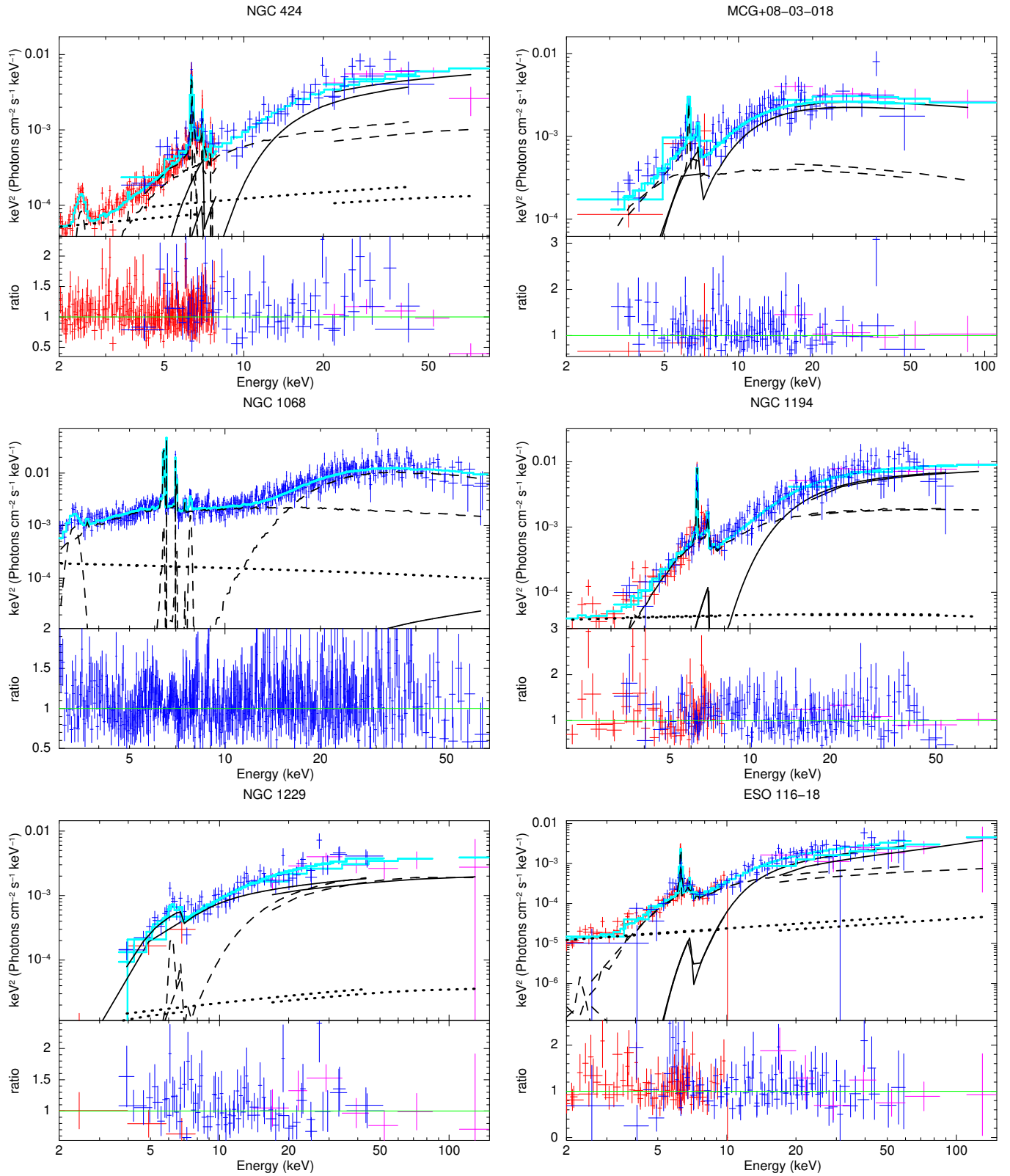


Figure 6. Background-subtracted spectra (top panel) and data-to-model ratio (bottom) of the CT-AGNs analyzed in this work using *borus02* with the covering factor as a free parameter. 2–10 keV data are plotted in red, *NuSTAR* data in blue and *Swift*-BAT data in magenta. The best-fitting model is plotted as a cyan solid line, the AGN main continuum is plotted as a black solid line, while the reprocessed component modelled by *borus02* and other additional emission lines are plotted as a black dashed line. Finally, the main power law component scattered, rather than absorbed, by the torus is plotted as a black dotted line.

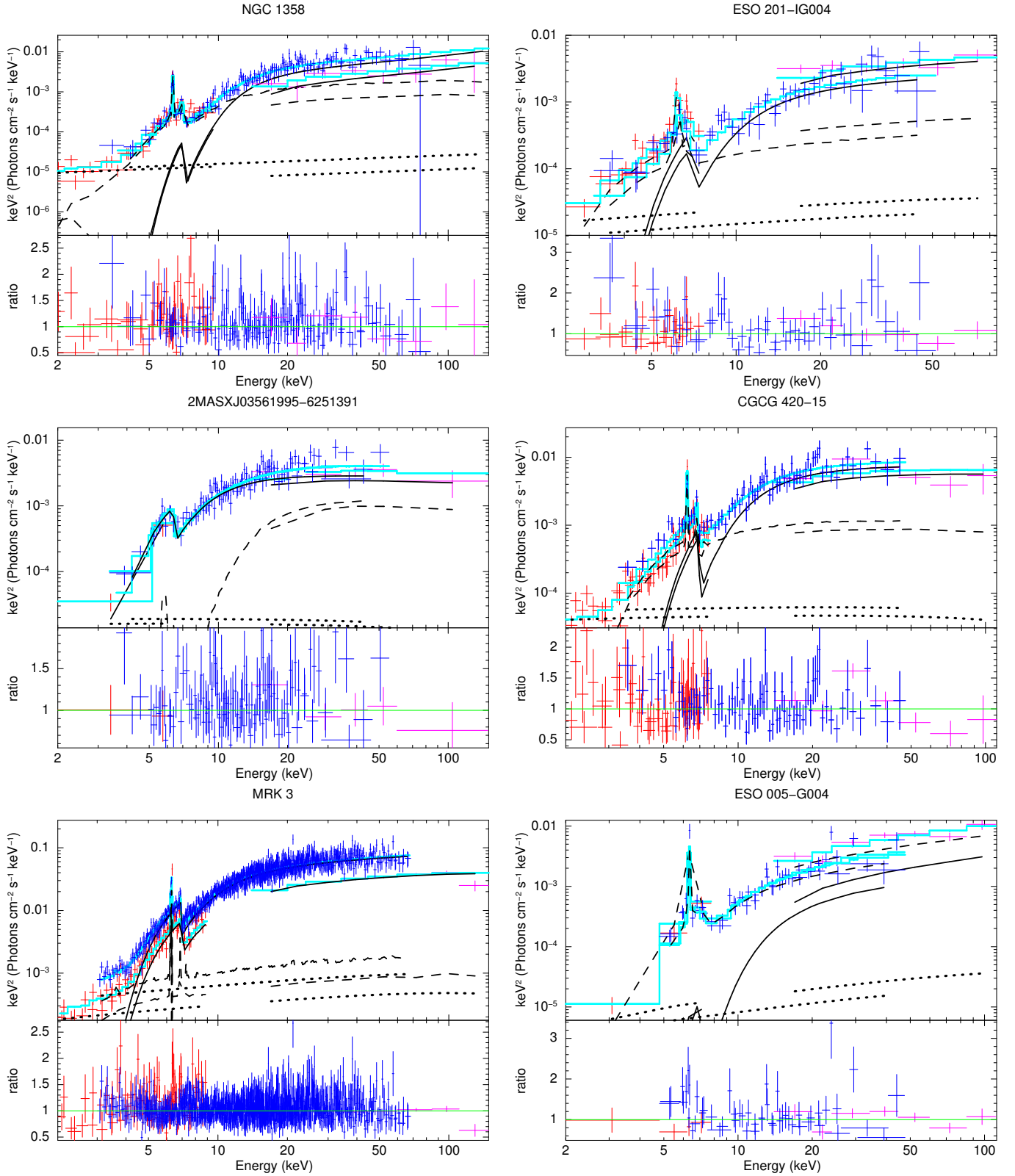


Figure 7. Background-subtracted spectra (top panel) and data-to-model ratio (bottom) of the CT-AGNs analyzed in this work using *borus02* with the covering factor as a free parameter. 2–10 keV data are plotted in red, *NuSTAR* data in blue and *Swift*-BAT data in magenta. The best-fitting model is plotted as a cyan solid line, the AGN main continuum is plotted as a black solid line, while the reprocessed component modelled by *borus02* and other additional emission lines are plotted as a black dashed line. Finally, the main power law component scattered, rather than absorbed, by the torus is plotted as a black dotted line.

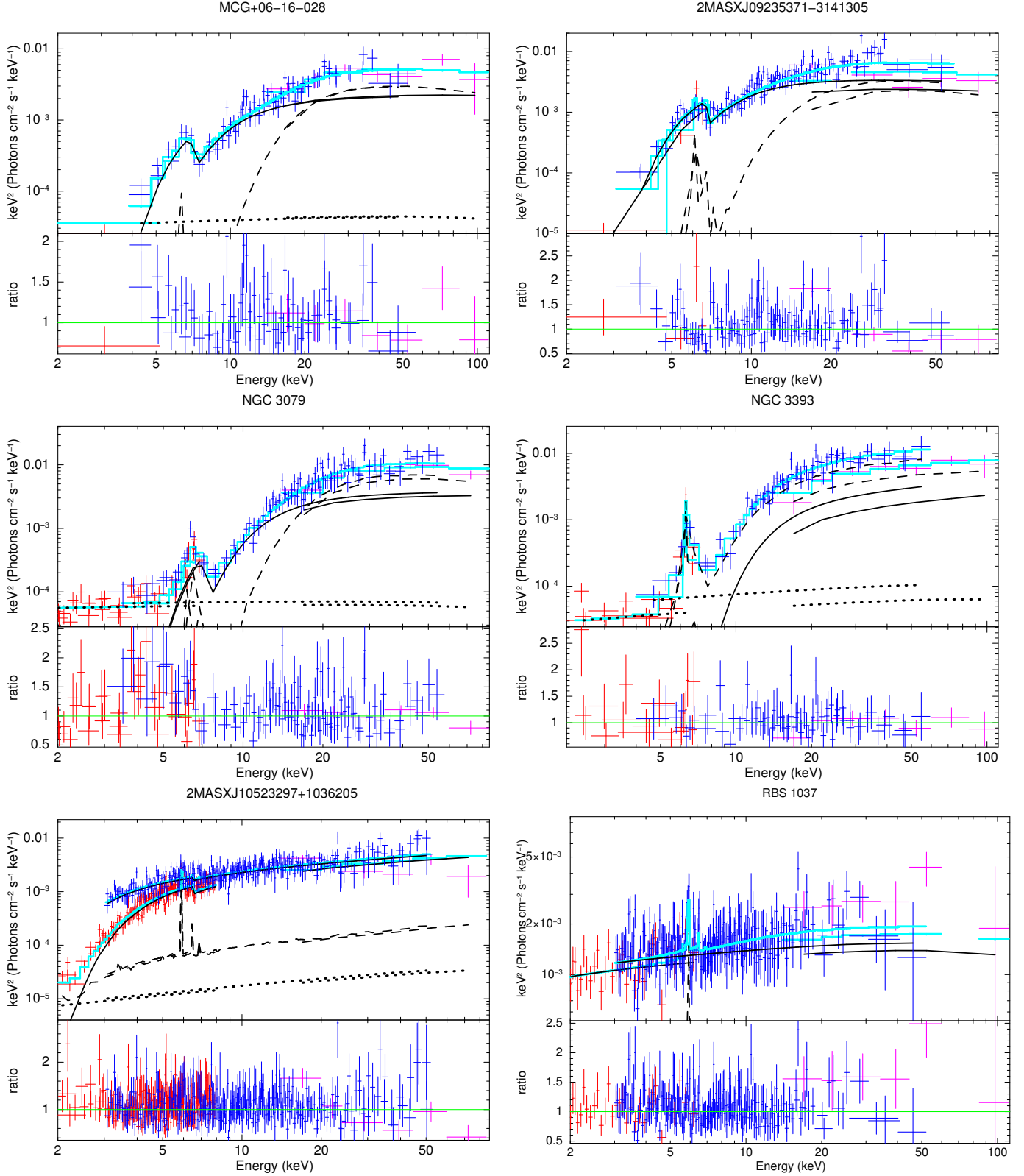


Figure 8. Background-subtracted spectra (top panel) and data-to-model ratio (bottom) of the CT-AGNs analyzed in this work using *borus02* with the covering factor as a free parameter. 2–10 keV data are plotted in red, *NuSTAR* data in blue and *Swift*-BAT data in magenta. The best-fitting model is plotted as a cyan solid line, the AGN main continuum is plotted as a black solid line, while the reprocessed component modelled by *borus02* and other additional emission lines are plotted as a black dashed line. Finally, the main power law component scattered, rather than absorbed, by the torus is plotted as a black dotted line.

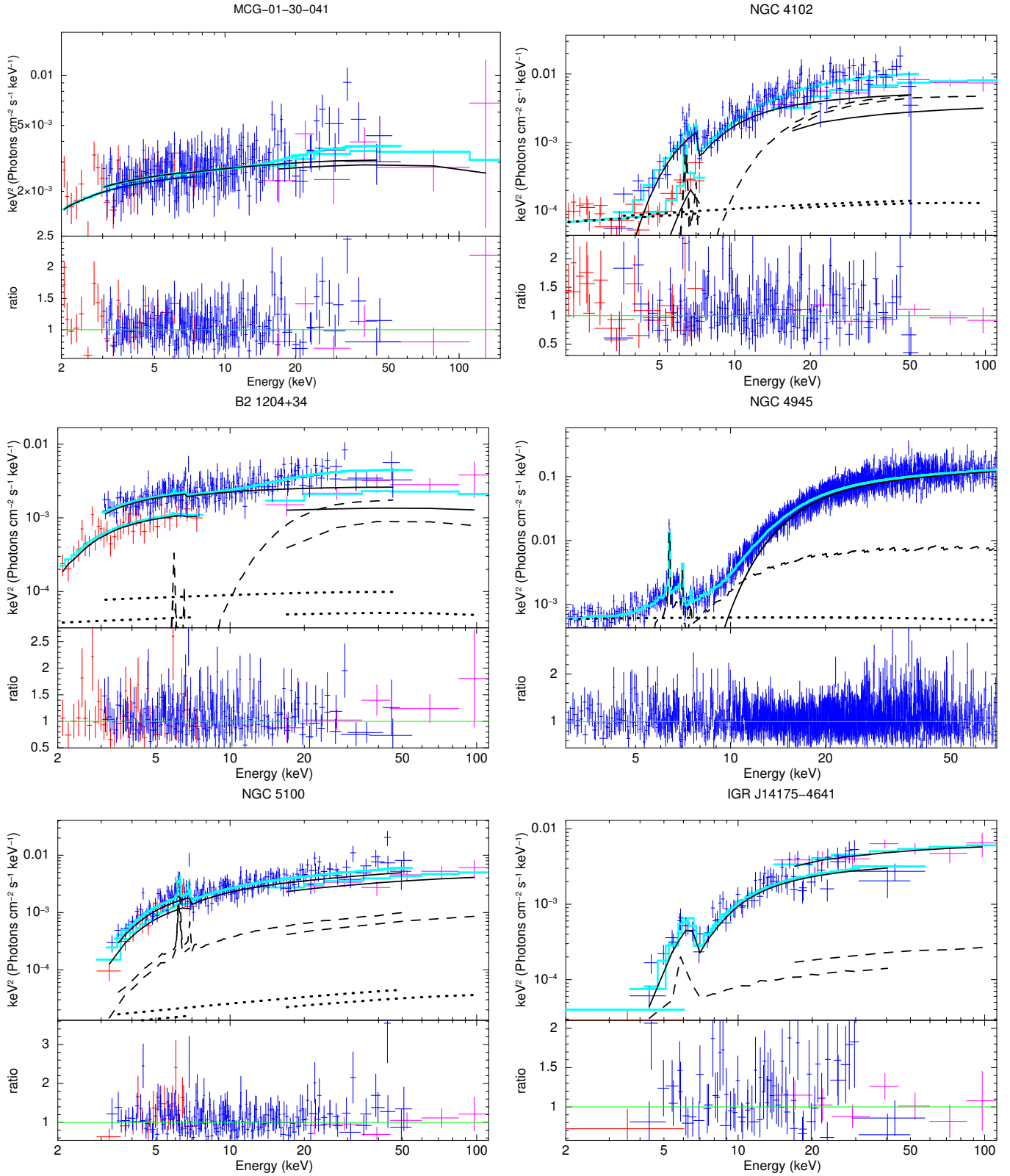


Figure 9. Background-subtracted spectra (top panel) and data-to-model ratio (bottom) of the CT-AGNs analyzed in this work using *borus02* with the covering factor as a free parameter. 2–10 keV data are plotted in red, *NuSTAR* data in blue and *Swift*-BAT data in magenta. The best-fitting model is plotted as a cyan solid line, the AGN main continuum is plotted as a black solid line, while the reprocessed component modelled by *borus02* and other additional emission lines are plotted as a black dashed line. Finally, the main power law component scattered, rather than absorbed, by the torus is plotted as a black dotted line.

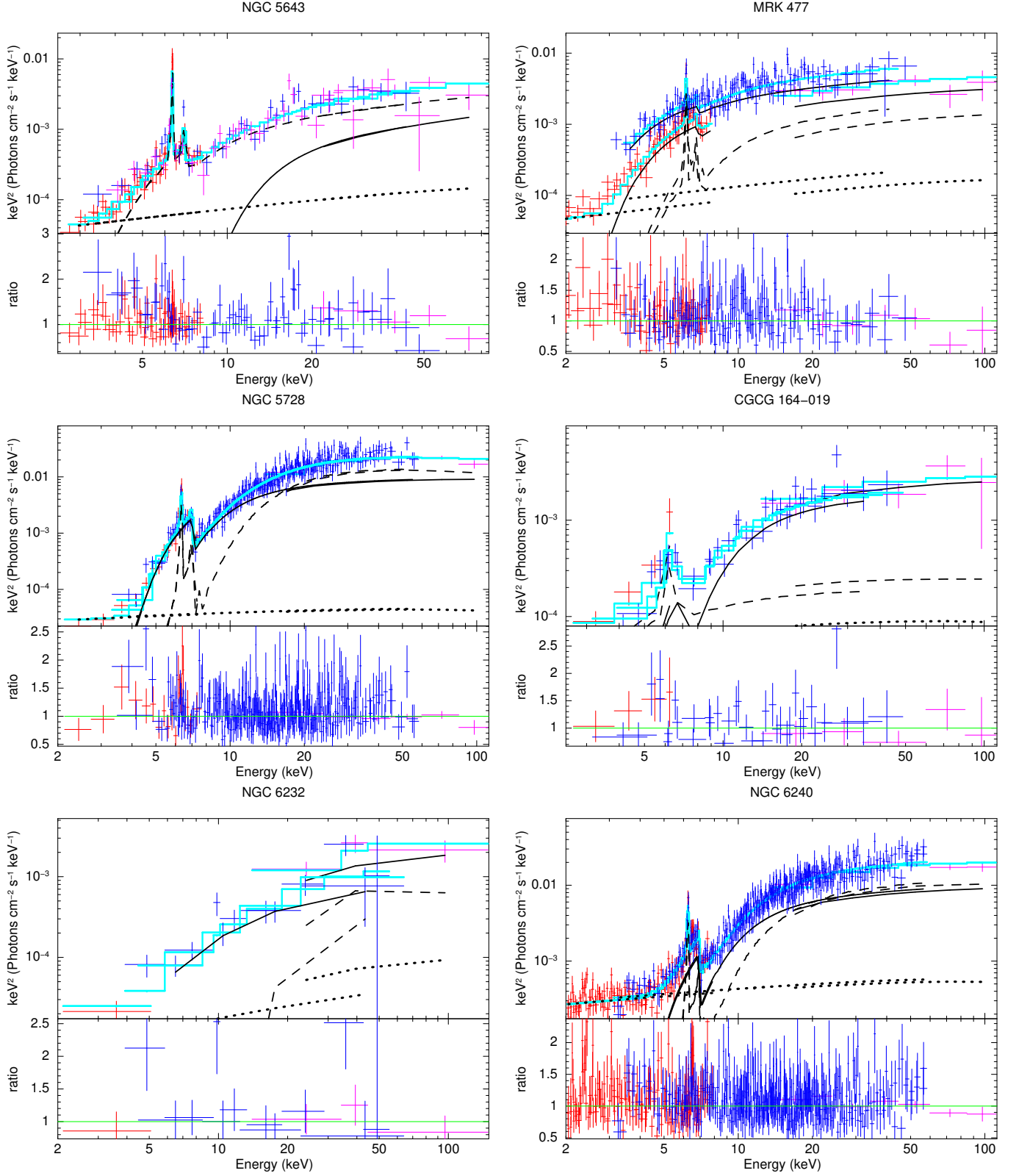


Figure 10. Background-subtracted spectra (top panel) and data-to-model ratio (bottom) of the CT-AGNs analyzed in this work using *borus02* with the covering factor as a free parameter. 2–10 keV data are plotted in red, *NuSTAR* data in blue and *Swift*-BAT data in magenta. The best-fitting model is plotted as a cyan solid line, the AGN main continuum is plotted as a black solid line, while the reprocessed component modelled by *borus02* and other additional emission lines are plotted as a black dashed line. Finally, the main power law component scattered, rather than absorbed, by the torus is plotted as a black dotted line.

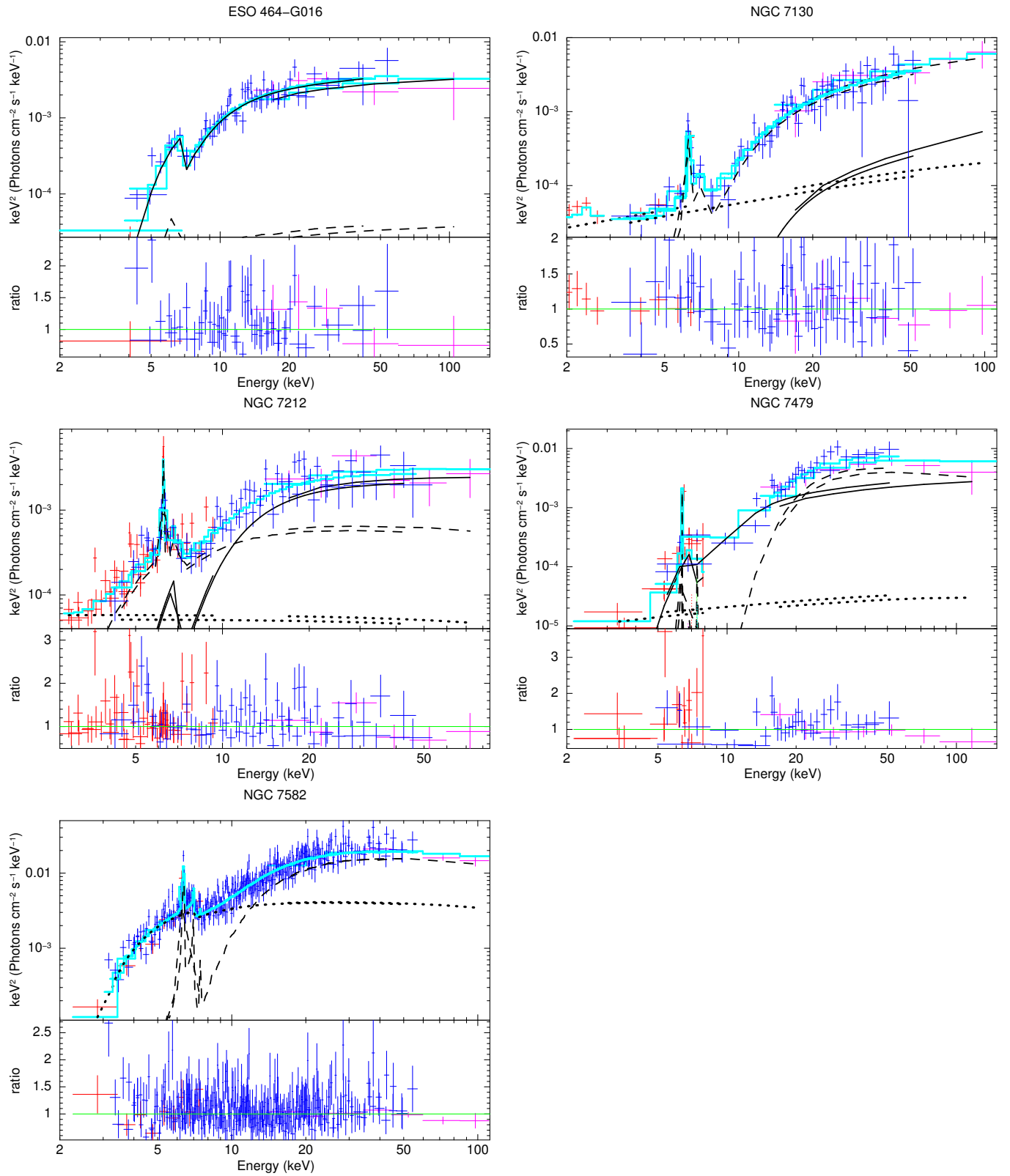


Figure 11. Background-subtracted spectra (top panel) and data-to-model ratio (bottom) of the CT-AGNs analyzed in this work using *borus02* with the covering factor as a free parameter. 2–10 keV data are plotted in red, *NuSTAR* data in blue and *Swift*-BAT data in magenta. The best-fitting model is plotted as a cyan solid line, the AGN main continuum is plotted as a black solid line, while the reprocessed component modelled by *borus02* and other additional emission lines are plotted as a black dashed line. Finally, the main power law component scattered, rather than absorbed, by the torus is plotted as a black dotted line.

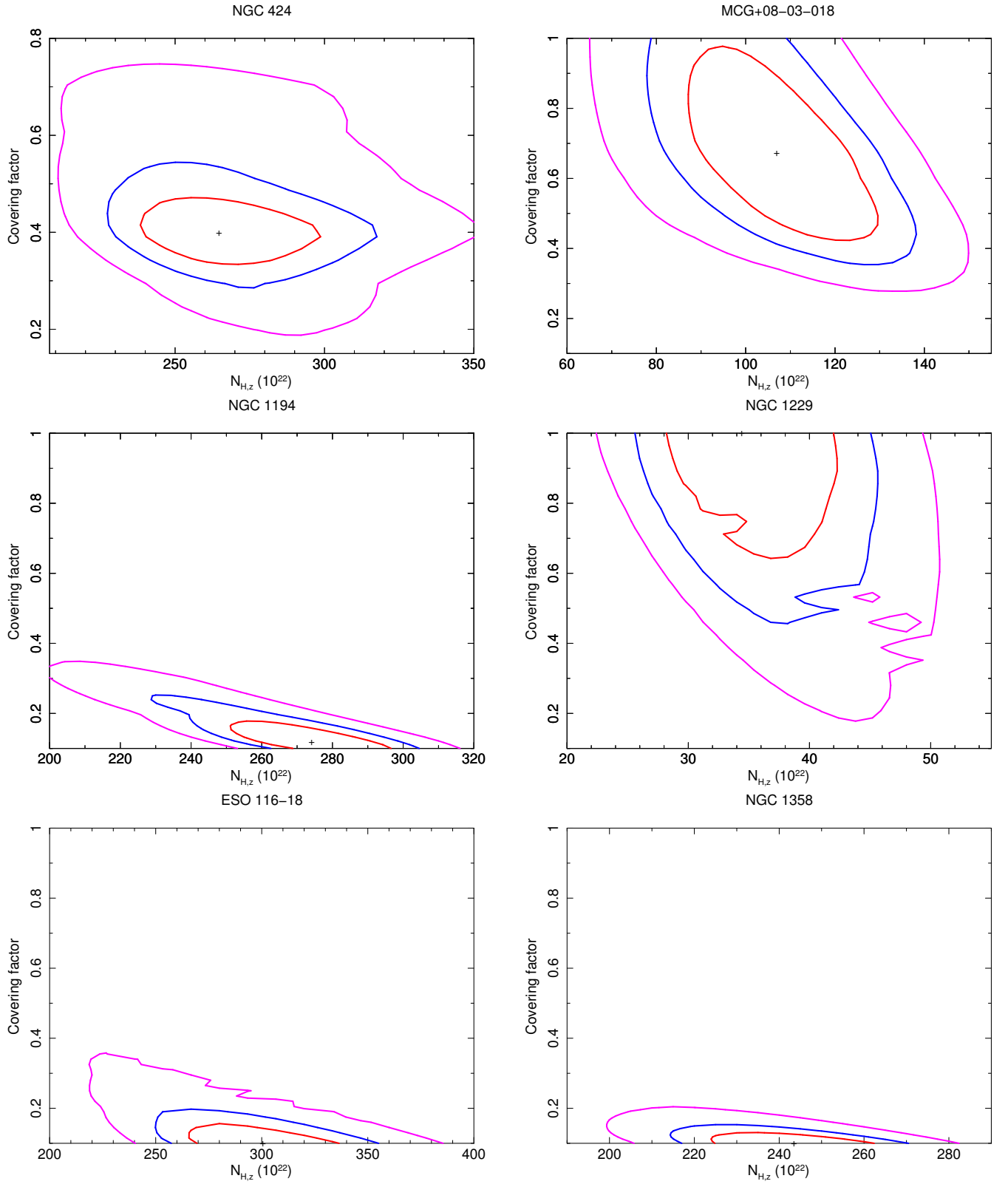


Figure 12. Confidence contours at 68, 90 and 99% confidence level for the line-of-sight column density, $N_{\text{H},z}$, and the torus covering factor, f_c , for six of the 35 sources analyzed in this work.

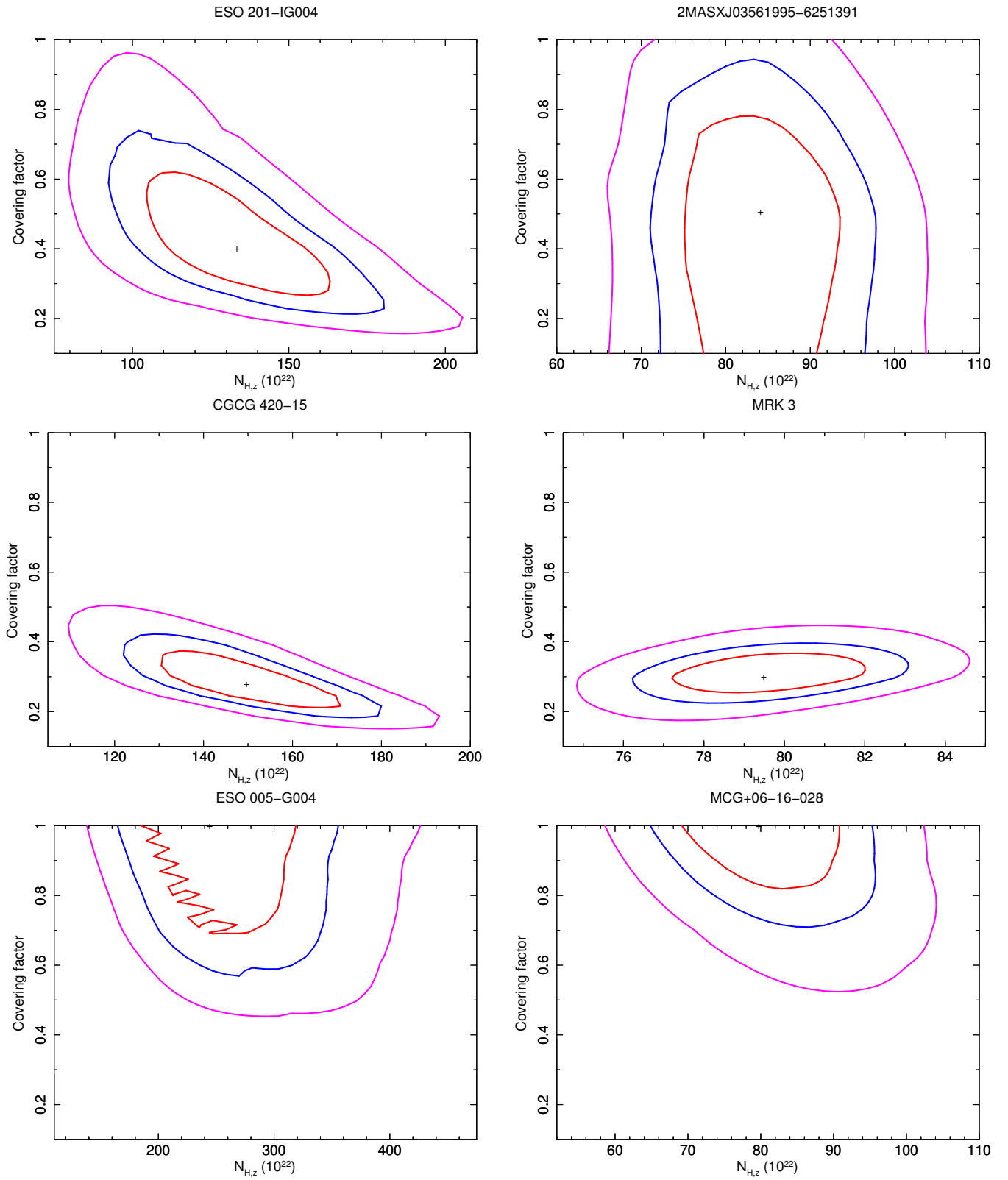


Figure 13. Confidence contours at 68, 90 and 99% confidence level for the line-of-sight column density, $N_{\text{H,z}}$, and the torus covering factor, f_c , for six of the 35 sources analyzed in this work.

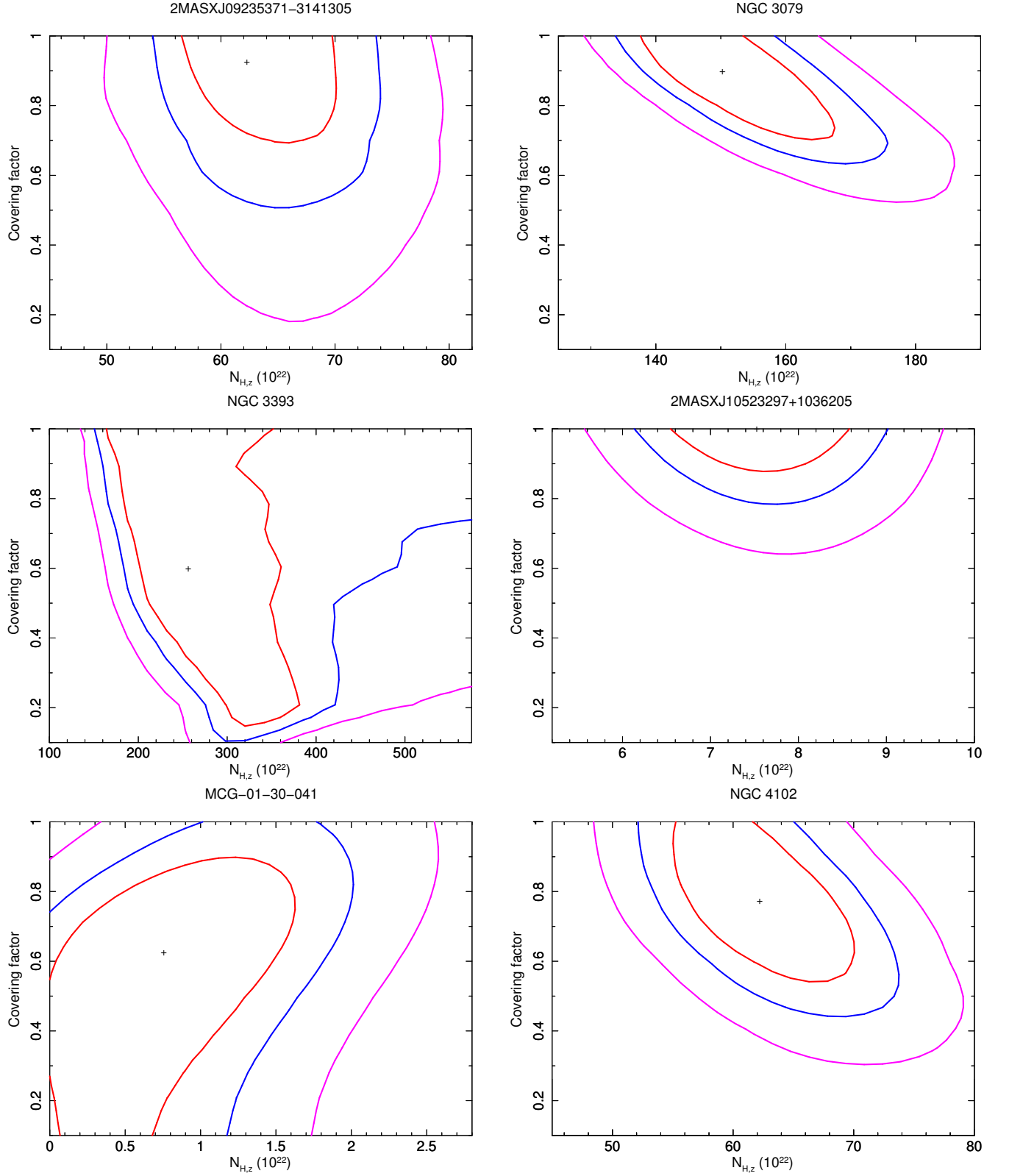


Figure 14. Confidence contours at 68, 90 and 99% confidence level for the line-of-sight column density, $N_{\text{H,z}}$, and the torus covering factor, f_c , for six of the 35 sources analyzed in this work.

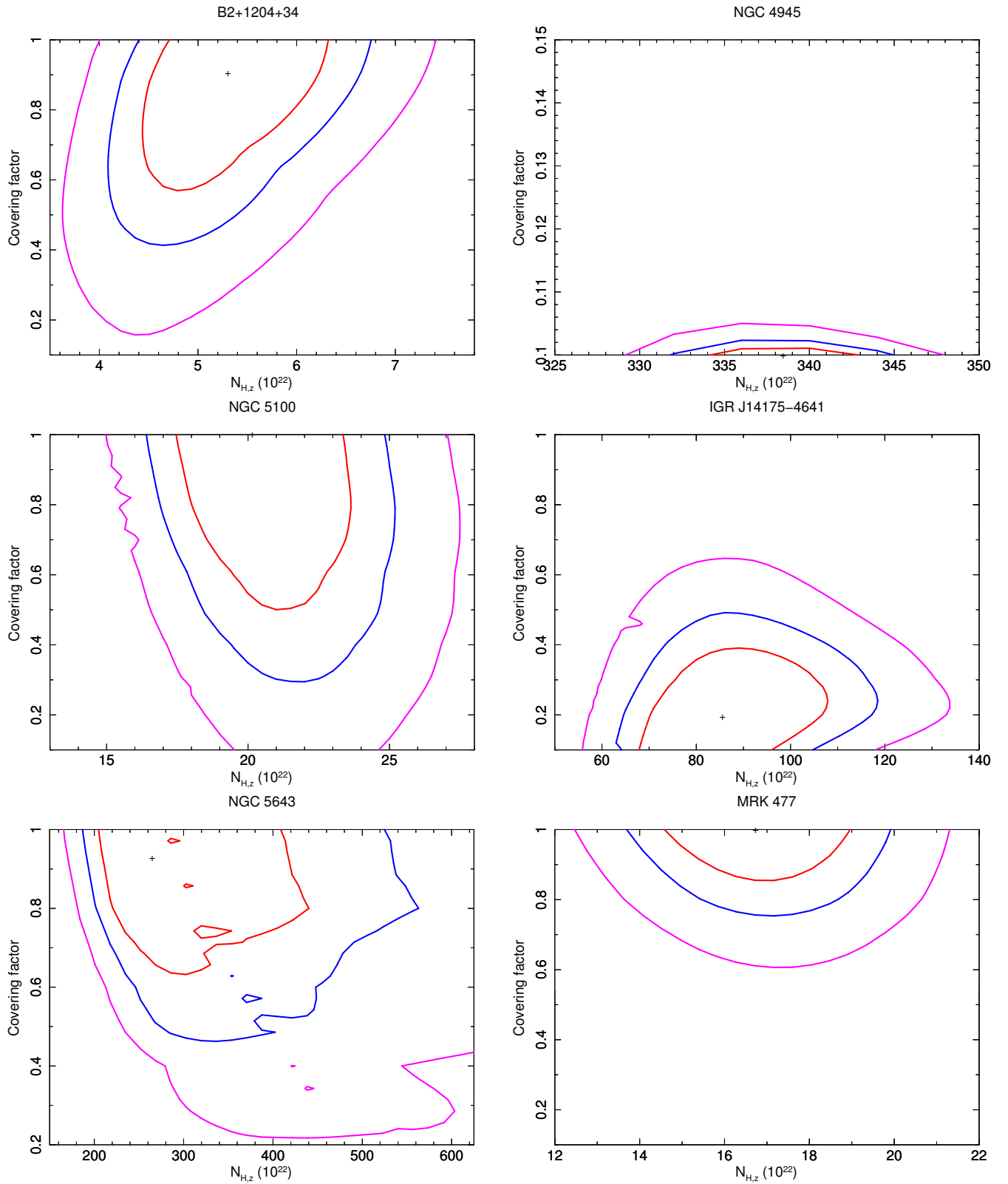


Figure 15. Confidence contours at 68, 90 and 99% confidence level for the line-of-sight column density, $N_{\text{H},z}$, and the torus covering factor, f_c , for six of the 35 sources analyzed in this work.

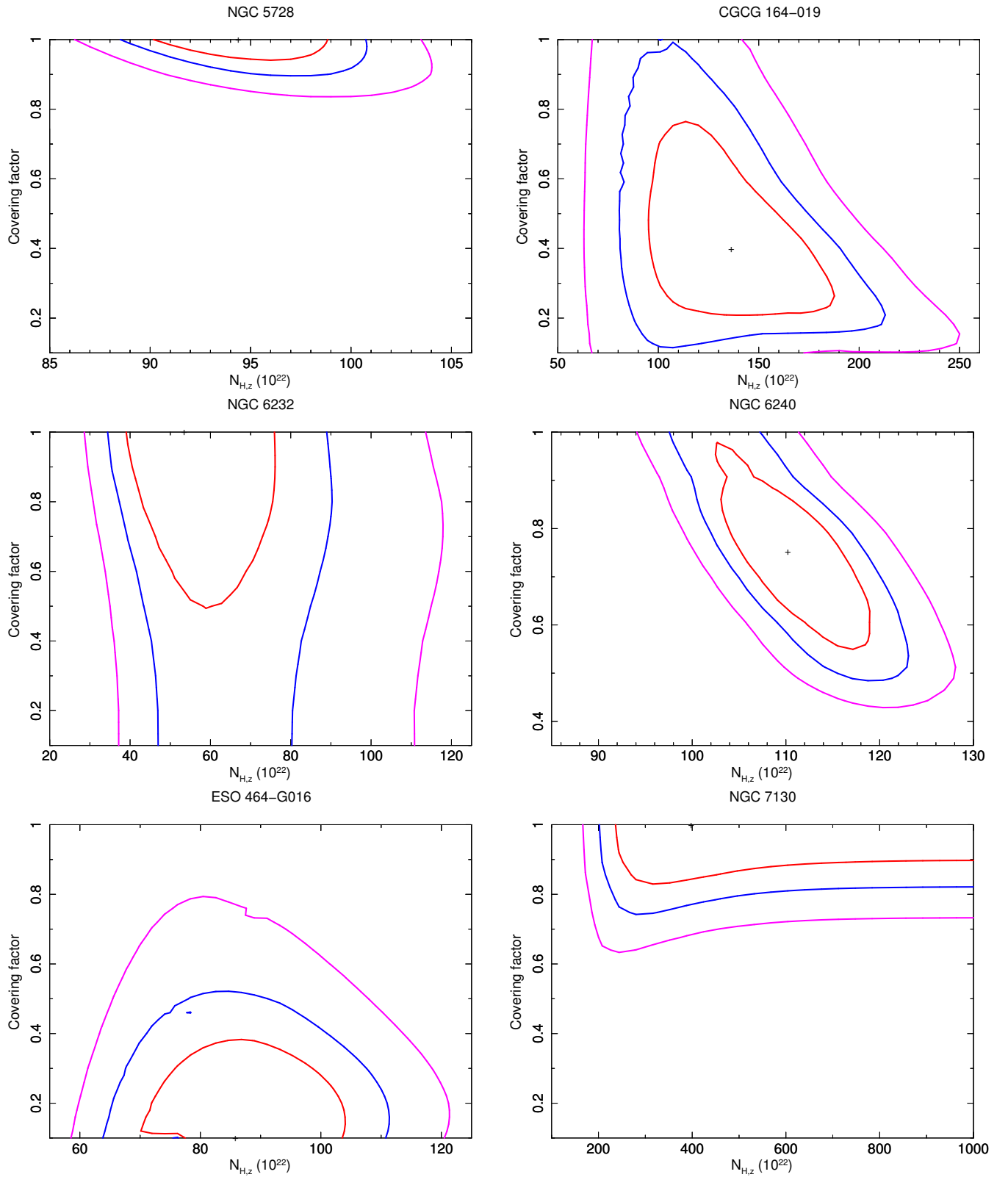


Figure 16. Confidence contours at 68, 90 and 99% confidence level for the line-of-sight column density, $N_{\text{H},z}$, and the torus covering factor, f_c , for six of the 35 sources analyzed in this work.

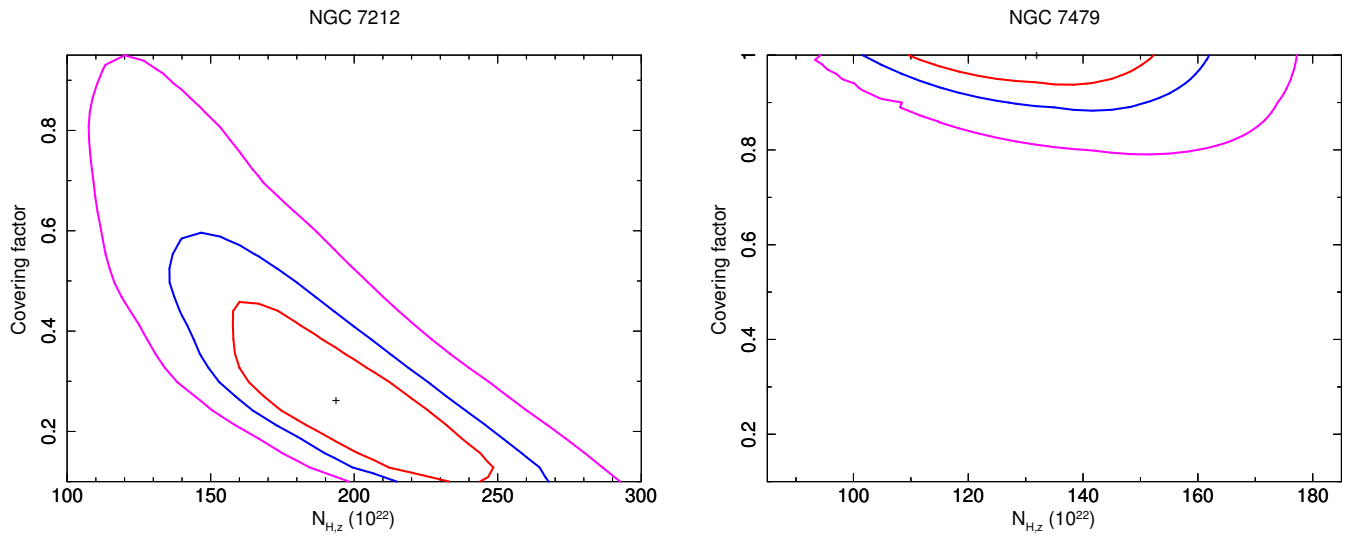


Figure 17. Confidence contours at 68, 90 and 99% confidence level for the line-of-sight column density, $N_{\text{H,z}}$, and the torus covering factor, f_c , for two of the 35 sources analyzed in this work.

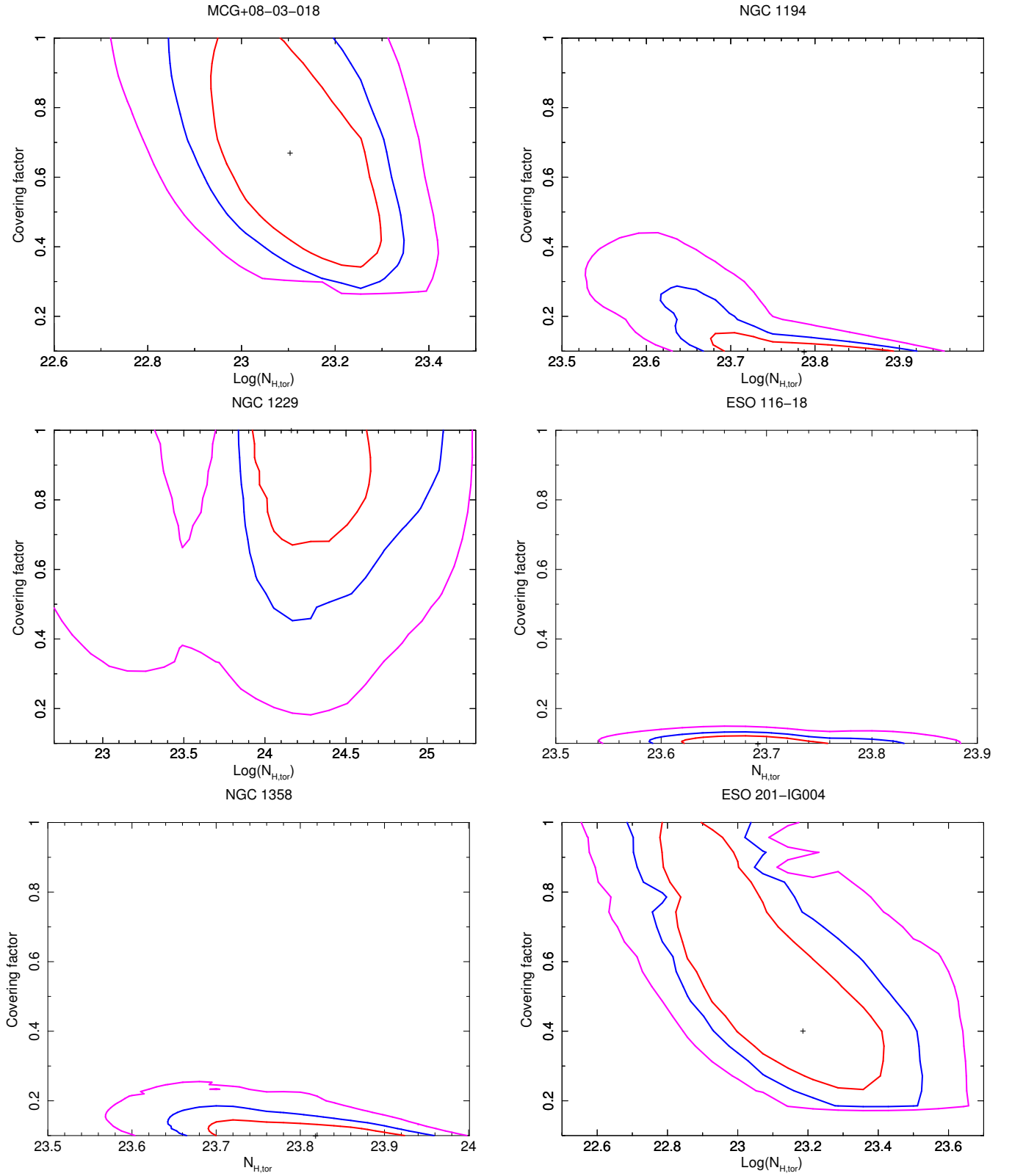


Figure 18. Confidence contours at 68, 90 and 99% confidence level for the torus average column density, $N_{\text{H,tor}}$, and the torus covering factor, f_c , for six of the 35 sources analyzed in this work.

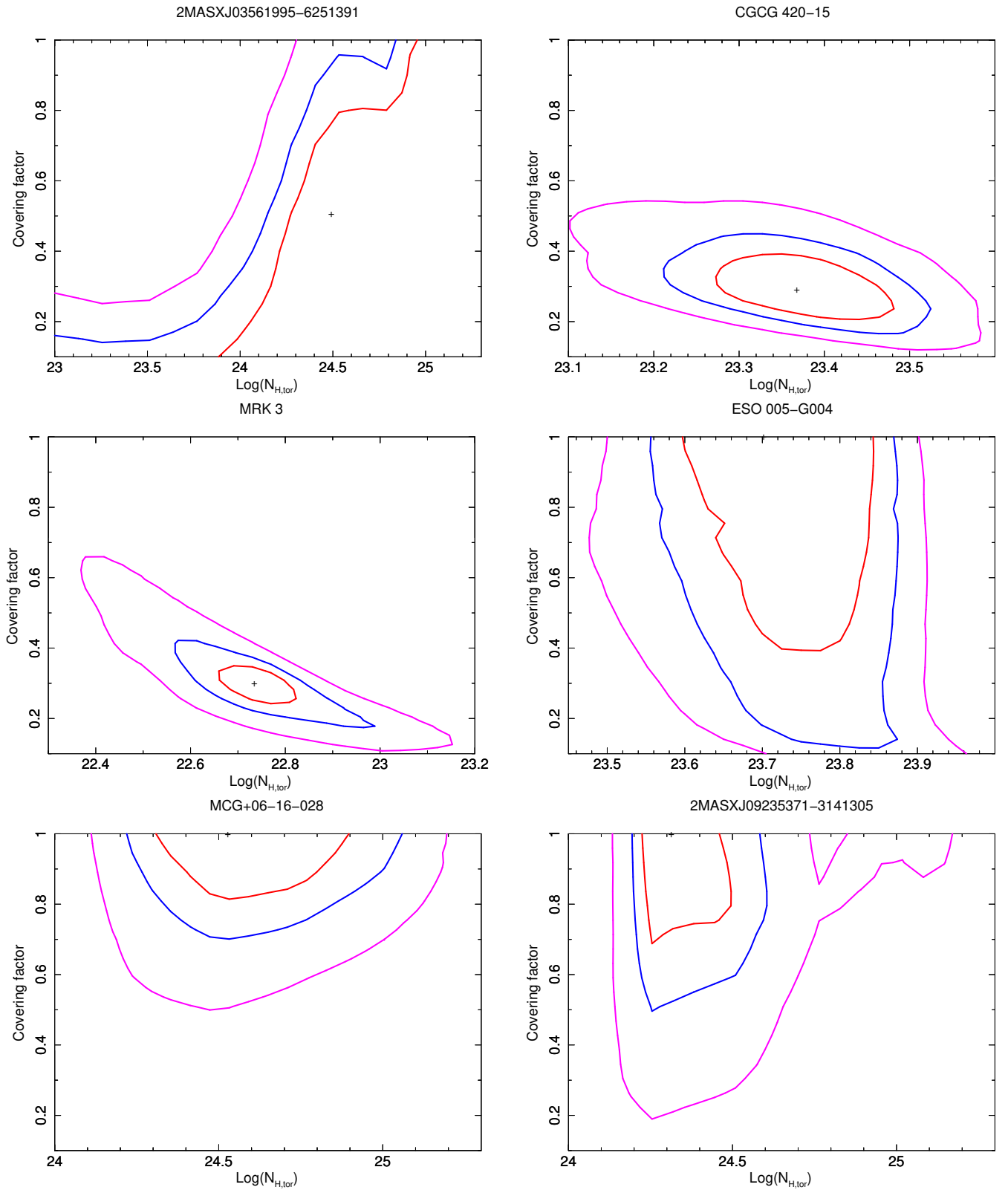


Figure 19. Confidence contours at 68, 90 and 99% confidence level for the line-of-sight column density, $N_{\text{H,z}}$, and the torus covering factor, f_c , for six of the 35 sources analyzed in this work.

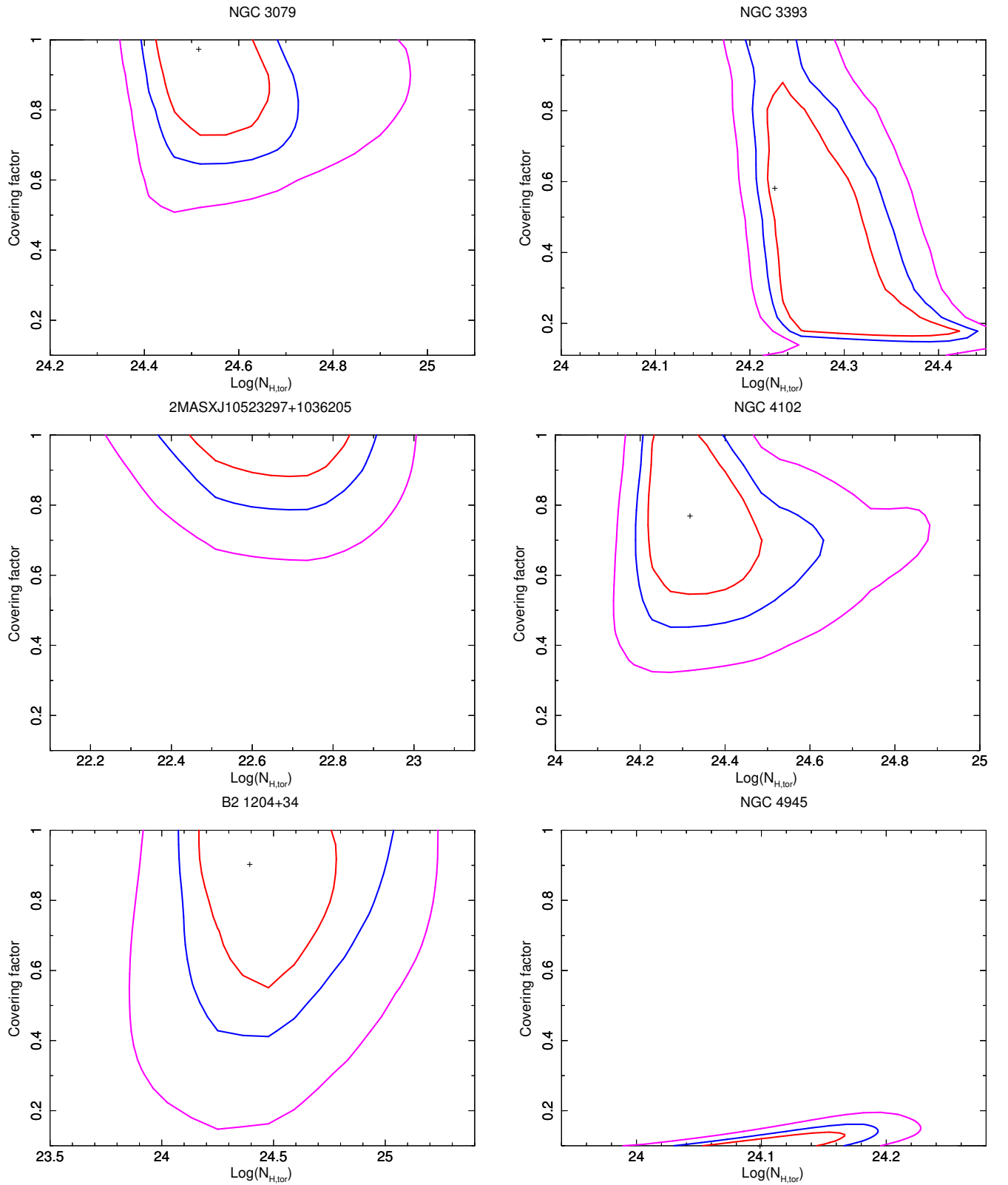


Figure 20. Confidence contours at 68, 90 and 99% confidence level for the line-of-sight column density, $N_{\text{H,z}}$, and the torus covering factor, f_c , for six of the 35 sources analyzed in this work.

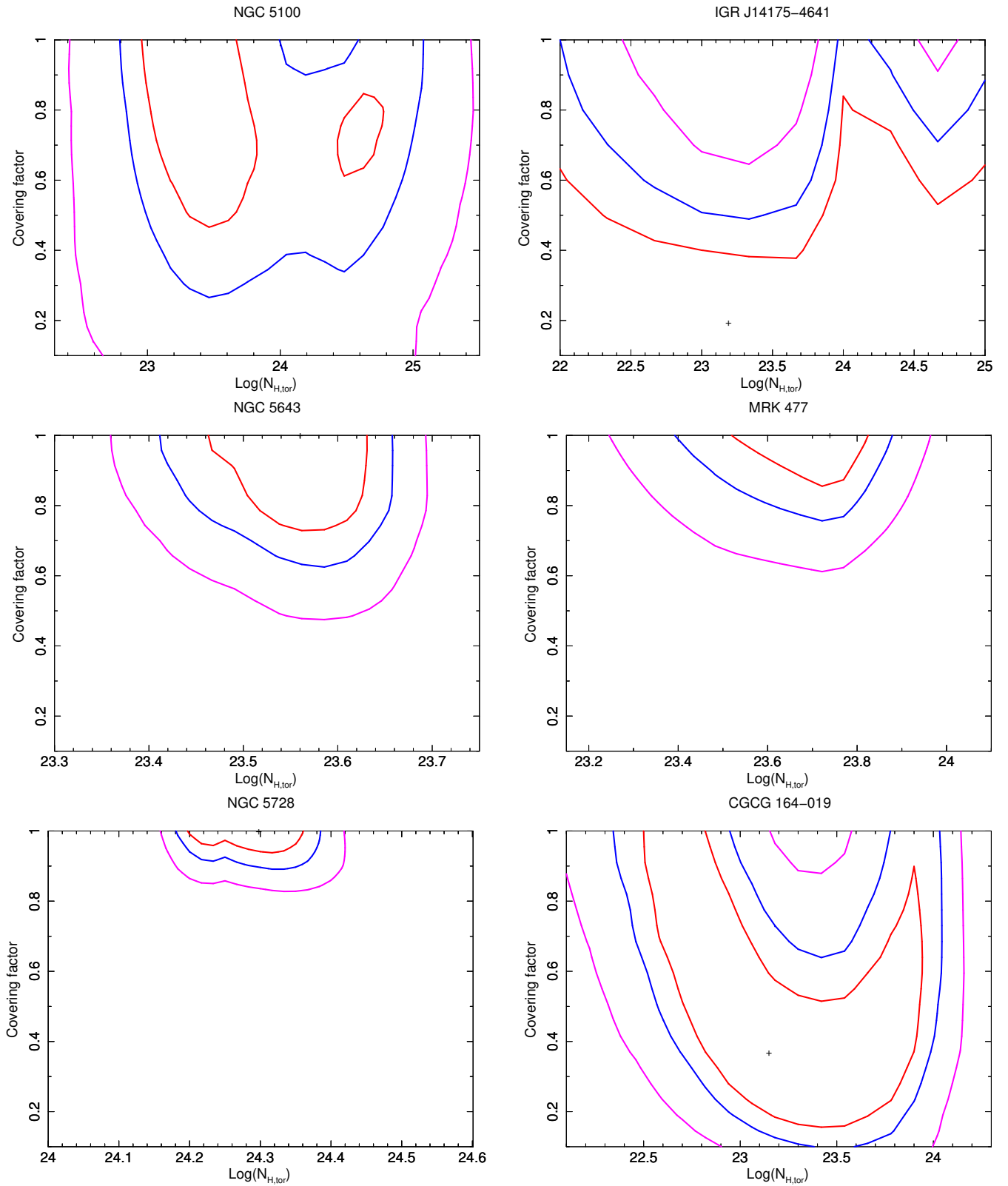


Figure 21. Confidence contours at 68, 90 and 99% confidence level for the line-of-sight column density, $N_{\text{H,z}}$, and the torus covering factor, f_c , for six of the 35 sources analyzed in this work.

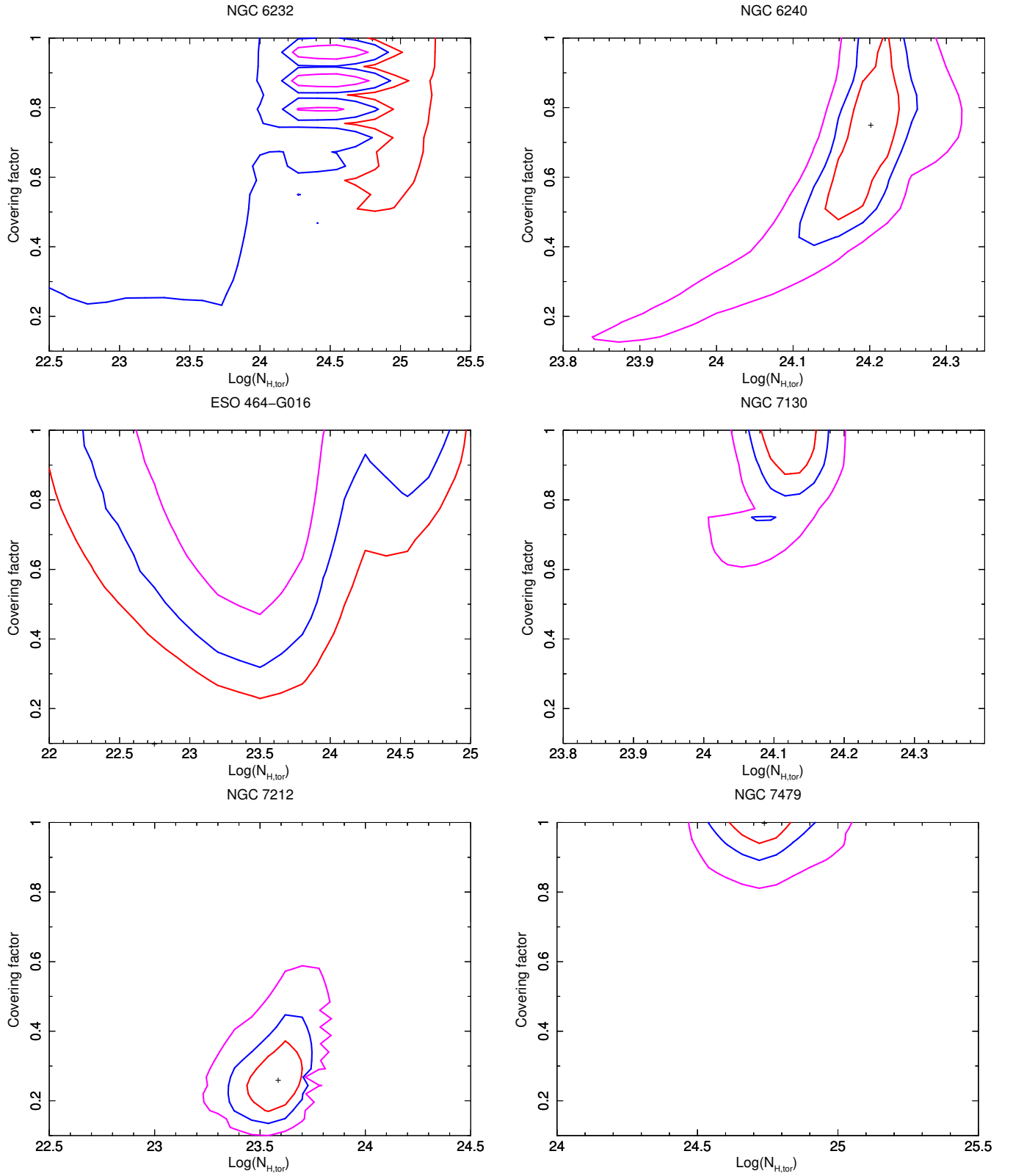


Figure 22. Confidence contours at 68, 90 and 99% confidence level for the line-of-sight column density, $N_{\text{H,z}}$, and the torus covering factor, f_c , for six of the 35 sources analyzed in this work.

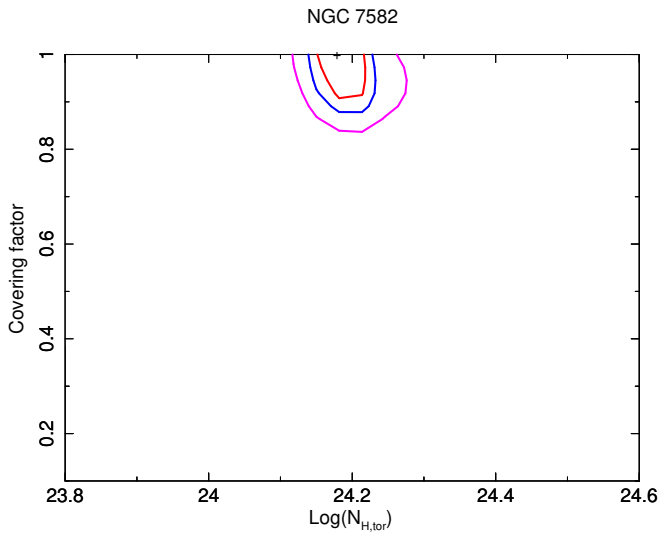


Figure 23. Confidence contours at 68, 90 and 99% confidence level for the line-of-sight column density, $N_{\text{H,z}}$, and the torus covering factor, f_c , for NGC 7582, one of the 35 sources analyzed in this work.

- Puccetti, S., Comastri, A., Bauer, F. E., et al. 2016, *A&A*, 585, A157
- Puccetti, S., Comastri, A., Fiore, F., et al. 2014, *ApJ*, 793, 26
- Ricci, C., Trakhtenbrot, B., Koss, M. J., et al. 2017a, *ApJS*, 233, 17
- Ricci, C., Trakhtenbrot, B., Koss, M. J., et al. 2017b, *Nature*, 549, 488
- Ricci, C., Ueda, Y., Koss, M. J., et al. 2015, *ApJL*, 815, L13
- Risaliti, G., Elvis, M., Fabbiano, G., Baldi, A., & Zezas, A. 2005, *ApJL*, 623, L93
- Risaliti, G., Elvis, M., Fabbiano, G., et al. 2007, *ApJL*, 659, L111
- Risaliti, G., Maiolino, R., & Salvati, M. 1999, *ApJ*, 522, 157
- Risaliti, G., Nardini, E., Salvati, M., et al. 2011, *MNRAS*, 410, 1027
- Rivers, E., Baloković, M., Arévalo, P., et al. 2015, *ApJ*, 815, 55
- Rowan-Robinson, M. 1995, *MNRAS*, 272, 737
- Segreto, A., Cusumano, G., Ferrigno, C., et al. 2010, *A&A*, 510, A47
- Severgnini, P., Caccianiga, A., & Della Ceca, R. 2012, *A&A*, 542, A46
- Simpson, C. 2005, *MNRAS*, 360, 565
- Taylor, M. B. 2005, in *Astronomical Society of the Pacific Conference Series*, Vol. 347, *Astronomical Data Analysis Software and Systems XIV*, ed. P. Shopbell, M. Britton, & R. Ebert, 29
- Tazaki, F., Ueda, Y., Terashima, Y., & Mushotzky, R. F. 2011, *ApJ*, 738, 70
- Vasudevan, R. V., Brandt, W. N., Mushotzky, R. F., et al. 2013, *ApJ*, 763, 111
- Verner, D. A., Ferland, G. J., Korista, K. T., & Yakovlev, D. G. 1996, *ApJ*, 465, 487
- Yaqoob, T. 2012, *MNRAS*, 423, 3360
- Yaqoob, T., Tatum, M. M., Scholtes, A., Gottlieb, A., & Turner, T. J. 2015, *MNRAS*, 454, 973
- Zhao, X., Marchesi, S., & Ajello, M. 2018a, arXiv e-prints [1812.05229]
- Zhao, X., Marchesi, S., Ajello, M., et al. 2018b, arXiv e-prints [1811.06027]